Doctoral Thesis

Circuit design of battery-less modules operated by Wiegand pulse

Wiegand パルスで駆動するバッテリーレス・モジュールの回路設計

Department of Mathematics, Physics, Electrical Engineering and Computer Science,
Graduate School of Engineering Science,
Yokohama National University

Xiaoya Sun　　孫 小雅

Thesis advisor: Professor Yasushi Takemura

July, 2021

要旨

IoT（Internet of Things）とは、すべてのモノがインターネットに接続される技術、またはそのような情報化社会を表す概念である。モノに記録されている情報や、各種センサから得られる情報をインターネットを経由して収集し、モノの状態や位置などを把握することが可能になろうとしている。今後、多種多様な場所、モノにセンサが設置されると予想され、電源の配線やメンテナンスが不要な自立型電源の活用が求められている。その解決策として身の周りに存在する微小なエネルギーを集め、発電するエネルギー・ハーベスティング（環境発電）への期待が高まっている。

本論文では、複合磁気ワイヤを用いる Wiegand センサを新たなエネルギー・ハーベスティング素子として活用することを提案し、その発電特性を明らかにした。このセンサは、外部磁界の時間変化率に依存しない、一定のパルス電圧を誘発するという特徴を有する。即ち、コイルに発生する誘導起電力は、それを貫く磁束の時間変化率に比例するというファラデーの電磁誘導に従わず、超低速の磁界変化に対してもパルス電圧を発生する。このパルス電圧を電子デバイスの駆動電源として利用したり、信号（パケット）の無線送信に必要な電力を賄うことができれば、電源配線や電池を必要としない無電源機器を実現できる。小型センサや無線モジュールと組み合わせることにより、電池交換や配線などが難しい場所でのセンシングを行うことが可能となる。メンテナンスフリーで長期間の運用が可能なため、IoT 分野での幅広い応用が期待される。

本論文の目的は、Wiegand センサが誘発するパルス電圧により電子機器を駆動する整流・平滑回路を明らかにすること、及び汎用性の高い発電素子として活用する手法を明らかにすることである。そこで、Wiegand センサの内部インダクタンス及び intrinsic なパルス電圧を算出し、発電素子としての特性を評価した。具体的には、Wiegand センサに接続した負荷回路の電圧・電流応答を実測し、電気回路モデルを構築、シミュレータ MATLAB®/Simulink®を用いて Wiegand センサの内部インダクタンス及び intrinsic なパルス電圧を決定した。Wiegand センサを等価電源として記述できるようになったために、それに接続する回路を LTspice®を用いて設計することが初めて可能になった。最適なデバイスの選定及びパラメータの算出を行うことにより、自励式昇圧回路を設計し、安定な直流 5 V を出力する方法を見いだし、それを測定により実証した。

このように本論文では、Wiegand センサを発電素子として実用する指針を提示することに成功した。ここで得られた Wiegand センサ及びその接続回路に関する手法は、IoT を初めとした広範な応用が想定され、エレクトロニクス分野において意義のある研究成果である。

Table of Contents

Chapter 1: Introduction

1.1 Background

Through Internet of Things (IoT) technology, all entities can be connected to the Internet, and information from various sensors, including position and temperature sensors, can be collected through the Internet, allowing the states and positions of various objects to be controlled in real time. Additionally, IoT technology is used to collect information in various big data and artificial intelligence applications. Connected devices are typically referred to as IoT devices, and it is estimated that there will be approximately 35 billion IoT devices worldwide by the end of 2021. It is estimated that the number of IoT devices will increase rapidly, with data trends suggesting that the number will reach anywhere from 80 to 120 billion by 2025.[1] For example, IoT devices will be installed in streets to count the number of pedestrians on the road, or in regions that are difficult for humans to access, to understand the ecology of plants and animals. A significant number of sensors are expected to be installed in the coming years for various applications. However, it is difficult to supply power to sensors at all times.[2] Therefore, self-applying power-driven sensors that do not require maintenance are required.[3, 4] Furthermore, as the number and size of sensor networks increase, the replacement of exhausted batteries becomes more time-consuming and wasteful. As a solution, energy harvesting technology is attracting significant attention because low quantities of energy from pressure and radio waves can be harvested and converted into electrical energy.[5, 6]

Figure 1.1 presents the modules of a typical IoT application. Sensors (including temperature, position, or acceleration sensors) can be installed in appliances and devices used in daily life, such as air conditioners, cell phones, and autonomous cars. We can then obtain relevant information from sensors through network connections and remotely control devices. In a living environment, various sensors for measuring environmental characteristics can be installed. These sensors require a large amount of power. With continued development in terms of miniaturization and energy saving, small power supplies can meet the demands of various IoT sensor applications.[7–9] Renewable energy generation is also a viable method that continues to supply power as long as there is energy in the surrounding environment.[10, 11] Therefore, a sensor using renewable energy can be installed with an independent power source for a long period of time without replacing a power harness or batteries. In this study, we used a Wiegand sensor with a composite magnetic wire as a novel energy-harvesting element to implement power generation through electromagnetic induction.

A Wiegand sensor, which contains a magnetic wire, has special features that cannot be realized by other magnetic sensors. For example, the output voltage does not depend on the rate of change of external magnetic fields, a wide operating temperature range is allowed, and the sensor is operable without a power supply.[12, 13] In particular, because it generates a constant pulse voltage, even in a magnetic field with ultra-slow-speed changes, this sensor is called a zero-speed sensor.[14] For practical applications, a power supply that combines a Wiegand sensor with a bicycle odometer has been developed.[15] A Wiegand sensor can be installed on the front fork or other components of a bicycle and a magnet can be mounted on the wheel of the bicycle. The rotation of the bicycle wheel generates a Wiegand effect, resulting in the generation of an output pulse voltage. These pulses can be used to power a non-volatile counter-integrated circuit. Additionally, Wiegand sensors can be used to power ultra-low-power displays (such as LCD watch displays) that present counts.[16]

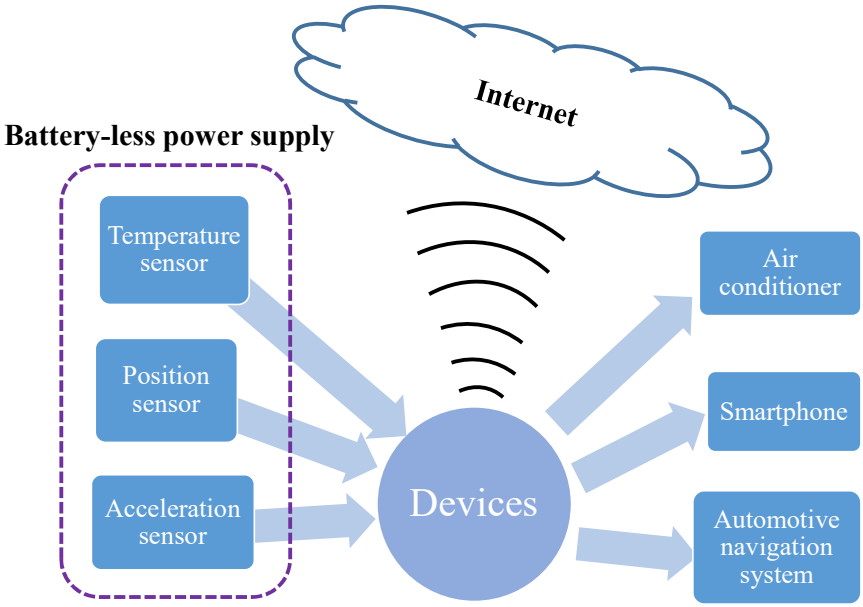

Figure 1.1 Concepts of an IoT system.

Based on these features, a Wiegand sensor can be used as a power source for a motor rotation counter,[17] or to drive the power supply of an electronic device. Furthermore, if the wireless transmission power required for signals (packets) can be covered, a wireless module can be realized by combining a Wiegand sensor with another small sensor. This makes it possible to perform sensing in places where it is difficult to replace batteries or harnesses. Therefore, these sensing modules can be operated for a long time without maintenance and are expected to be used extensively in the IoT field.

Figure 1.2 presents a map of applications using Wiegand sensors in an IoT system. The range of sensing equipment required for IoT applications is wide, including environment-related illuminance, temperature, and physical state sensors for switch status detection or of the opening and closing of doors and windows. The data collected by these sensors are uploaded to the Internet via wireless communication, and they can be viewed on a computer or smartphone. The most important advantage of energy harvesting using Wiegand sensors for IoT devices is that no batteries, external power sources, or maintenance are required. As a result, costs related to construction, power consumption, and maintenance can be reduced. Therefore, IoT devices can be installed in harsh locations to collect various types of data. Another advantage is that data can be retrieved semi-permanently and without maintenance, even when IoT devices are located in harsh environments. Ideally, IoT devices should be installable anywhere, and they should be able to send useful data at all times in harsh environments.

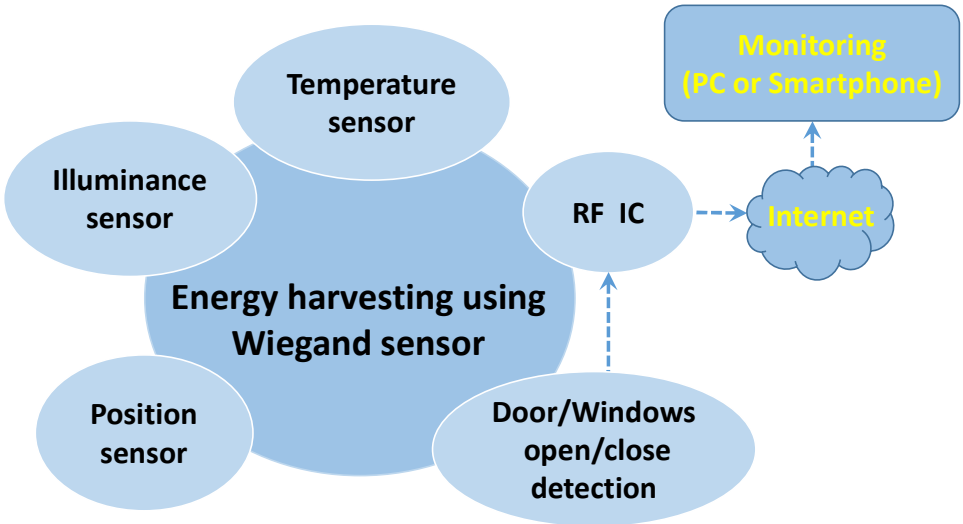

Figure 1.2 Energy harvesting using Wiegand sensors in an IoT system.

Recently, energy harvesting technology that yields outputs in the order of microwatts to watts has been attracting significant attention.[18, 19] Such technology is expected to be used as independent power supplies for small electronic devices.[20, 21] As shown in Figure 1.3, the power generated by an energy harvester varies significantly depending on the type of harvester source.[9] Solar cells can generate 1 W of power or more in a sunny outdoor environment, but the power generated by indoor light is significantly lower. Similarly, the amount of power generated by thermal energy and vibration energy fluctuates significantly with changes in the surrounding environment. Therefore, power sources for energy harvesting are generally unstable. However, power generation using Wiegand sensor is not affected by the external environment. Such sensors can be installed anywhere to obtain continuous and stable energy. The energy generated by Wiegand sensors is small, but it can be practically used for IoT devices with low energy consumption. When an IoT system does not transmit data, the system runs in a standby operation mode (sleep mode) with low power consumption. Therefore, Wiegand systems are expected to be used continuously and stably as power sources for IoT systems with low power consumption.

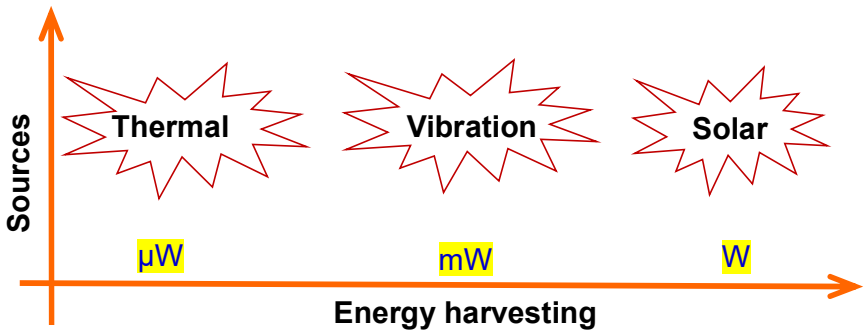

Figure 1.3 Power range of energy harvesting and energy sources.

1.2 Research Objectives and Main Contributions

In a Wiegand sensor, the output voltage does not depend on the external magnetic field and a constant output voltage pulse is induced, even by an ultra-slow magnetic field change.[22] This output voltage pulse can be used as a power source for electronic devices and is expected to be used as an independent power supply for small devices such as IoT sensors.[23, 24] Therefore, in this study, we used the electromagnetic induction method for a Wiegand sensor, which induces a frequency-independent pulse voltage, to develop battery-less power generation modules.

As shown in Figure 1.4, to realize the application of energy harvesting using Wiegand sensors in IoT systems, it is necessary to feed power into IoT devices such as sensors, radio frequency integrated circuits (RF ICs), and RF wireless sensors. Based on the latest research results, the minimum power consumption of a temperature sensor is 1.99 μW.[25] Therefore, it is practically significant to develop an energy harvesting method that generates a power of 2 μW. However, considering the power consumption of the electrical circuit connected to a power supply and sensor, the power supply circuit should be optimized in terms of its consumed power. Additionally, it is also necessary to realize a stable voltage in a short time immediately after operation begins, to stabilize the system quickly. Therefore, a method to obtain a low-power-consuming circuit with a fast response was researched in this study.

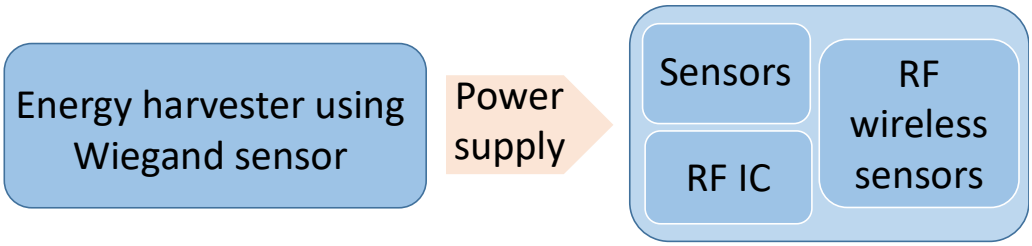

Figure 1.4 Energy harvesting using Wiegand sensors for IoT devices.

The pulse voltage from a Wiegand sensor must be converted into a DC power voltage for IoT devices. A Wiegand sensor, which consists of a pick-up coil wound around a composite magnetic wire, has internal resistance and inductance values. Therefore, it is necessary to clarify the features of the intrinsic output voltage (V_{in}) of Wiegand sensors. In this study, V_{in} was successfully determined by calculating the internal resistance and inductance values according to the characteristics of Wiegand sensors. LTspice® was used to simulate circuit responses. V_{in} was derived by optimizing the parameters of the circuits used in our experiments. Additionally, a self-oscillating boost converter circuit was designed to generate a stable DC output voltage of 5 V. Various properties of the boosted output voltage were clarified in our experiments. Based on this theoretical and experimental research, an electrical circuit with a stable output and fast response was successfully designed. A power supply in the order of 2 μW using Wiegand sensors was achieved. This supply could be used as a power source for low-power-consuming electronic devices and modules such as IoT sensors.

1.3 Organization of this Thesis

In this study, the pulse voltage generated by a Wiegand sensor was converted into a DC voltage and used as a power supply for IoT devices. After the characteristics of the Wiegand sensor were clarified, an AC-DC converter circuit for converting the pulse voltage into DC voltage was analyzed. An equivalent circuit model of the Wiegand sensor was designed to enable the simulation of the circuit responses related to the Wiegand sensor. Finally, a DC booster circuit was designed and its performance was analyzed through calculations and experiments. The organization of this thesis is illustrated in Figure 1.5.

The background and purpose of this study are discussed in Sections 1.1 and 1.2 of Chapter 1. In Chapter 2, the magnetic properties of the magnetic material and operating principles of the Wiegand sensor are discussed.

In Chapter 3, the calculation of the internal inductance, resistance, and waveform of the intrinsic pulse voltage (V_{in}) of the Wiegand sensor are described. The determination of V_{in} is significant because it enables circuit simulation using LTspice® for developing a circuit connected to a Wiegand sensor.

In Chapter 4, the design and performance of a self-oscillating boost converter circuit based on the results described in Chapter 3 are discussed. A boosted DC voltage of 5 V is experimentally obtained. This method can be used for power supplies in various device modules. Finally, Chapter 5 summarizes the results of this study.

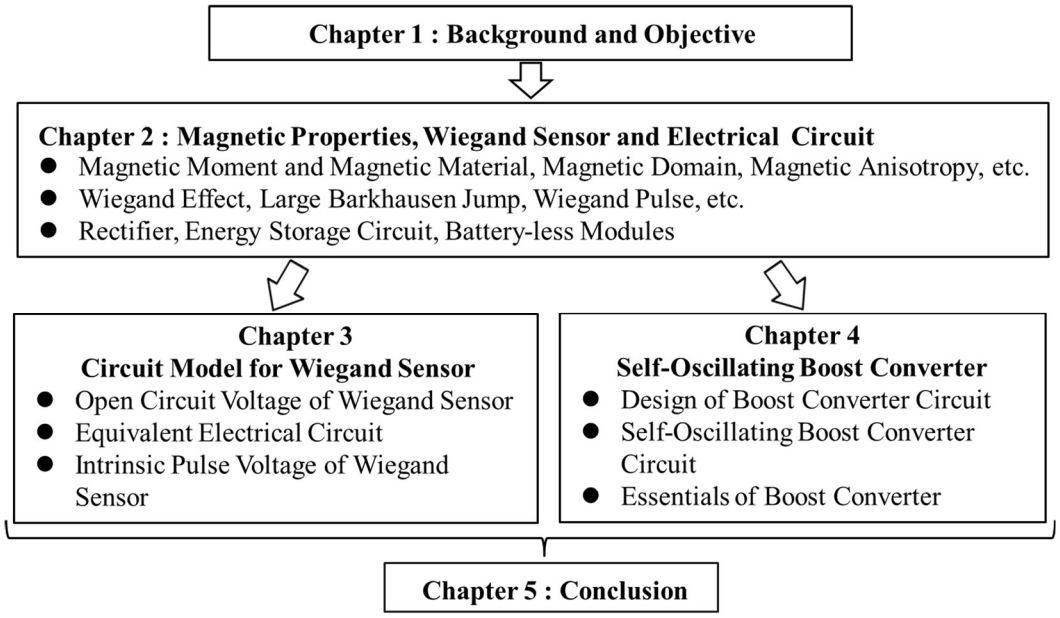

Figure 1.5 Organization of this thesis.

Chapter 2: Theories

2.1 Magnetic Properties

2.1.1 Magnetic Moment and Magnetic Material

The magnetic moment represents a pair of positive and negative magnetic poles. It describes the magnetic properties of a circular current in a coil or microscopic magnetization. The origin of the magnetic moment is usually considered to be the motion of the electric charge and spin of the electron. A substance with a magnetic moment is called a magnetic material. The magnetic moment per unit volume is called magnetization. The unit of magnetization intensity is [Wb/m^2] or [T].

Because different materials have different electronic arrangements, materials show different features in a magnetic field. In general, magnetic materials are classified as paramagnetic, ferromagnetic, antiferromagnetic, and ferrimagnetic.[26]

In paramagnetic materials, the directions of the magnetic moments are random owing to thermal fluctuations, as shown in Figure 2.1. When a magnetic field is applied, the magnetic moments are aligned in the same direction as the magnetic field. This response of the magnetic moment to the applied magnetic field is described by Langevin's theory. When the applied magnetic field is removed, the magnetic moments return to a random state.

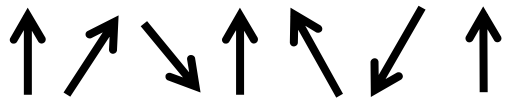

Figure 2.1 Magnetic moments in paramagnetic materials.

In ferromagnetic materials, the magnetic moments are aligned in the same direction, as shown in Figure 2.2, even when an external magnetic field is not applied. These aligned magnetic moments are the origin of spontaneous magnetization in ferromagnetic materials.

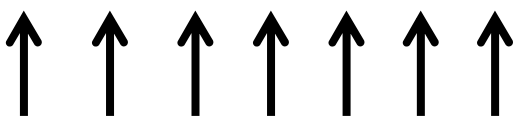

Figure 2.2 Magnetic moments in ferromagnetic materials.

Magnetic dipole interaction is not the origin of the alignment of magnetic moments in ferromagnetic materials, because the energy is smaller than the strength of the molecular magnetic field. Here, the exchange interaction is discussed to explain the alignment of magnetic moments. Specifically, two adjacent atoms, i and j, are assumed, and their magnetic moments of spin are S_i, and S_j, respectively. Moreover, their potential energy (binding energy), called the exchange interaction, is described by Equation (2.1). This equation determines the directions of S_i and S_j. This exchange interaction was effective between two adjacent atoms.

$$w_{ij} = -2J_{\mathrm{ex}} S_i \cdot S_j \tag{2.1}$$

(J_{ex}: exchange integral)

When $J_{\mathrm{ex}} > 0$, the parallel configuration of S_i and S_j exhibited the lowest energy. This is a ferromagnetic state.

As for the antiferromagnetic materials, adjacent magnetic moments are opposite in direction to each other, as shown in Figure 2.3, and do not exhibit magnetization as a whole. This antiparallel arrangement of magnetic moments can be understood by the exchange interaction with $J_{\mathrm{ex}} < 0$. When the temperature is higher than a certain degree, the directions of the magnetic moments become random, which is similar to those in paramagnetic materials.

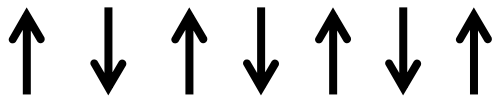

Figure 2.3 Magnetic moments in antiferromagnetic materials.

The arrangement of the magnetic moments in ferrimagnetic materials is similar to that in antiferromagnetic materials; however, the magnitudes of the adjacent magnetic moments are different. These magnetic moments are not canceled, and the material demonstrates spontaneous magnetization as a whole, which is similar to the ferromagnetic material, as shown in Figure 2.4.

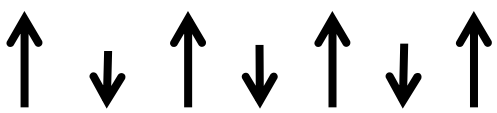

Figure 2.4 Magnetic moments in ferrimagnetic materials.

The response of magnetization as the total amount of magnetic moments to the externally applied magnetic field is significant. A magnetization *M*-*H* curve (hysteresis loop) of a ferromagnetic material is typically described as shown in Figure 2.5; here, *M* and *H* denote the amplitudes of magnetization and applied magnetic field, respectively. *M* is defined as the amplitude of magnetization in the direction of the applied magnetic field. Assume that the magnetization is zero under a zero magnetic field applied at the beginning. From this state of $M = 0$ at $H = 0$, an external magnetic field is applied. *M* increases with increasing *H*. *M* saturates at a certain intensity of the applied field, which is called the saturation magnetization (M_s). The magnetization process from the initial state of $M = 0$ at $H = 0$ is called the initial magnetization curve. Subsequently, even when the applied field intensity is reduced to $H = 0$, the magnetization process does not trace the initial magnetization curve. A certain intensity of *M* remains at $H = 0$, which is called the residual magnetization (B_r). When repeating the cycle of increasing and decreasing the applied field intensity, the magnetization process exhibits hysteresis. The intensity of the applied field with $M = 0$ is called the coercive force (H_c). These magnetization processes can be explained by the features of the magnetic domain, which will be introduced later.

Here, the process of realizing the initial magnetization state of $M = 0$ at $H = 0$ is described. This removal of magnetization in a magnetic material is called "degaussing." Once the ferromagnetic material is magnetized from the initial state, the magnetization will not normally return to the original state of $M = 0$, even when the applied magnetic field is removed. There are two major methods for degaussing. The first method uses an alternating magnetic field. After the magnetization is saturated by *H* of a sufficiently large intensity, the alternating field is applied repeatedly, while simultaneously reducing its intensity (amplitude). When the intensity is gradually reduced to zero, the materials are expected to exhibit $M = 0$. The second method heats the magnetic material above the Curie temperature. The direction of the magnetic moments becomes random at temperatures above the Curie temperature. Subsequently, the material exhibits $M = 0$ after it is cooled without any applied magnetic field.

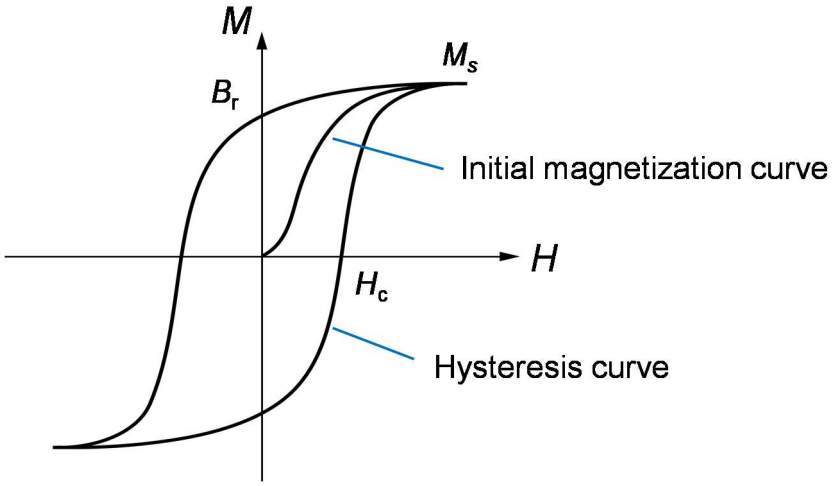

Figure 2.5 Hysteresis loop of ferromagnetic material.

The unit for the magnetic field intensity (strength) is [A/m]. Oersted [Oe] is also used for the magnetic field intensity in a cgs system (1 A/m = $4\pi/10^3$ Oe). Tesla [T] and Gauss [G] are the units of magnetic flux density in SI and cgs systems, respectively; 1 T = 10^4 G.

2.1.2 Magnetic Domain

Electrons move around the atomic nucleus, and a magnetic field is generated owing to this current for each atom. Therefore, it can be said that there are several magnetic moments at the atomic level in a material. The region of the material, which includes magnetic moments moving in the same direction, is called the magnetic domain. The boundary between the domains is called the domain wall. In magnetic materials, there are generally many magnetic domains with different orientations (of magnetic moments). Even in case where there are multiple magnetic domains with different orientations in ferromagnetic materials, it does not show magnetization as a whole, because the magnetic moments of different domains cancel each other out. When an external magnetic field is applied, the magnetic moments in the domain change their direction to be the same as the applied magnetic field. Additionally, the area of the magnetic domain, whose magnetic moments are parallel to the direction of the applied magnetic field, will increase, to minimize the total energy. This process is accompanied by the movement of the domain walls.[28] However, even becoming one domain at last, the domain direction is not exactly the same as the direction of the external magnetic field, unless the magnetic field strength is increased to a certain level, as shown in Figure 2.6.

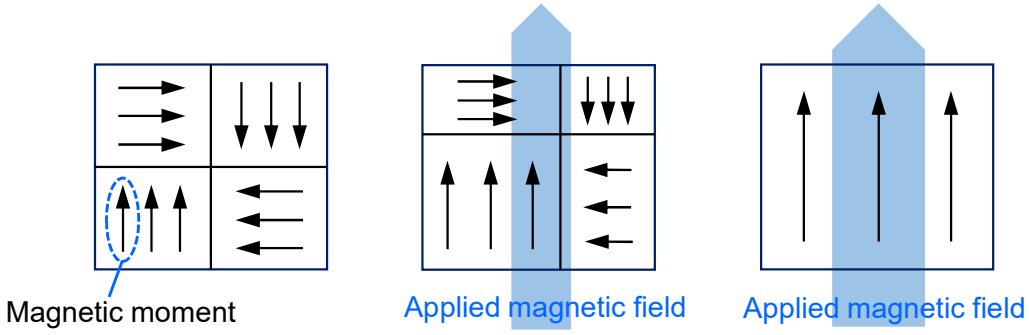

Figure 2.6 Change in magnetic domain structure under the applied magnetic field.

2.1.3 Demagnetizing Field and Magnetostatic Energy

In magnetic materials that are uniformly magnetized in one direction, positive and negative magnetic poles appear at both ends of the material. A Coulomb force occurs between these magnetic poles, and the potential energy increases, which is called magnetostatic energy. When the directions of the magnetic moment are aligned, the magnetostatic energy increases, resulting in an unstable state. Under these conditions, magnetic poles exist on the edge or surface of the magnetic material. To reduce the number of magnetic poles and magnetostatic energy, multiple magnetic domains are formed. Notably, the magnetic poles are the origin of the magnetic field.[27] When a magnetic material is magnetized in one direction, a magnetic field is generated from the positive to negative magnetic pole. This magnetic field exists both outside (leakage magnetic or stray field) and inside the material. The direction of the later magnetic field is opposite to the direction of magnetization, as shown in Figure 2.7. This magnetic field whose direction is opposite to that of the magnetization is called a demagnetizing field. The effect of this demagnetizing field cannot usually be ignored in ferromagnetic materials.

By considering this demagnetizing field, the intensity of the effective magnetic field (H_{eff}) applied to the magnetic material can be described as follows.

$$H_{\mathrm{eff}} = H - H_{\mathrm{d}} \tag{2.2}$$

The intensity of the demagnetizing field (H_{d}) can be calculated using the magnetization (J), as

$$H_{\mathrm{d}} = N\frac{J}{\mu_0} \tag{2.3}$$

where N is a constant with a value between 0 and 1, and is called the coefficient of the demagnetizing field (demagnetizing factor). When the value of N is large, it is necessary to apply a magnetic field of higher intensity to obtain the specific value of magnetization. Notably, N is determined by the shape of the material. When the material is thin, long, and magnetized in the longitudinal direction, N is small. Conversely, when the material is thick and short, N is large. It is not possible to calculate N accurately for magnetic materials with generally specific shapes. However, N can be calculated for several specific shapes of materials, such as materials with spheroid shapes.

In an orthogonal coordinate system, the coefficient of the demagnetizing field can be defined as the components of the x, y, and z axes, i.e., N_x, N_y, and N_z, respectively. These components satisfy Equation (2.4), and it is possible to estimate their approximate values depending on the shape of the material.

$$N_x + N_y + N_z = 1 \tag{2.4}$$

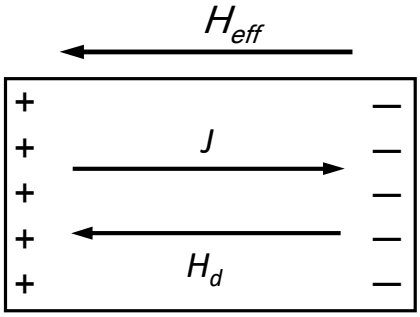

Figure 2.7 Demagnetizing field.

In this study, the Wiegand wire is typically in its dimensions of 0.25-mm diameter and 11-mm length. The demagnetizing field is in an axial direction, which is the effective direction of the externally applied magnetic field for exciting the wire.

2.1.4 Zeeman Energy

A magnetic material with magnetization M exhibits potential energy in an externally applied magnetic field H. As shown in Figure 2.8, this energy is called the Zeeman energy (E_z), and is described in Equation (2.5), where θ is the angle between M and H. The stable configuration of M and H with the lowest energy was realized by their parallel alignment. This is the physical mechanism for the change in direction of magnetization and magnetization reversal in magnetic materials.

$$E_z = -M \cdot H = -MH\cos\theta \tag{2.5}$$

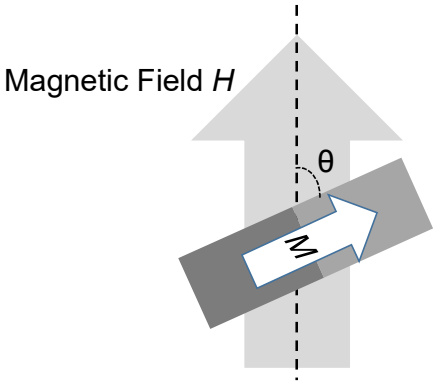

Figure 2.8 Zeeman energy.

As described in a later part in detail, the Wiegand wire exhibits a structure comprising two layers with different magnetic properties. By applying an external magnetic field, the magnetization directions of these two layers will change to either a parallel state or an antiparallel state. When the magnetization directions of the two layers are same in the parallel state, the magnetostatic energy is at its highest. By applying a magnetic field to change the magnetization configuration from the parallel to antiparallel state, the magnetostatic energy is reduced. Then, to revert to the parallel state, it is necessary to apply a relatively large magnetic field to reduce the Zeeman energy that is greater than the possible increase in the magnetostatic energy. The magnetization reversal of the Wiegand wire, including a large Barkhausen jump, is discussed in Section 2.2.4.

2.1.5 Magnetic Anisotropy

When the magnetic property of a magnetic material is measured by applying an external magnetic field, the magnetic properties vary depending on the direction of the applied field. Additionally, the magnetic material exhibits different characteristics along different directions (axis). These features are known as magnetic anisotropy. The potential energy, depending on the direction of observing the magnetic material characteristics, is called the magnetic anisotropy energy. When the lowest magnetic anisotropy energy is achieved in a specific direction of the magnetic material, the magnetization is easily oriented in this direction, and becomes stable; this is called the direction of the magnetic easy axis. Conversely, the direction with the highest magnetic anisotropy energy is called the direction of magnetic hard axis. The magnetization along this axis is unstable, and hardly occurs without an applied magnetic field.

There are several origins of magnetic anisotropy. Shape magnetic anisotropy is attributed to the different values of the demagnetizing field coefficient, depending on the direction of the magnetic material. The magnetic properties of single-crystal materials depend on the direction of the crystal axis of the magnetic material. For magnetic materials with magnetic anisotropy, when a magnetic field is applied along the direction of the magnetization easy axis, the magnetization is saturated by the applied magnetic field of low intensity. There will be some residual magnetization in the easy axial direction even when the applied magnetic field is removed. However, it is necessary to apply a magnetic field with a relatively high intensity to saturate the magnetization in the hard axial direction. There is almost no residual magnetization in the hard axial direction when the applied field is removed. These magnetization features cause the magnetization reversal process in the hysteresis curve, as shown in Figure 2.5.

In the case of the Wiegand wire, owing to its longitudinal wire shape, shape anisotropy is dominant. It has uniaxial anisotropy with an easy axis in the axial direction, and the radial direction shows a magnetically hard axis. Wiegand wires have a positive magnetostriction value. Therefore, uniaxial anisotropy is induced in the axial direction by the applied stress, and plastic deformation occurs, resulting in a lower coercive force near the surface rather than inside the wire due to twisting.[29, 30] It has been reported that the coercive force of the Wiegand wire decreases with an increase in the number of twist treatments.[31] After the twisting and annealing treatments, the Wiegand wire exhibits coercive fields of 2 and 8 mT/μ_0 in the outer surface and inner center regions, respectively. The details of the magnetic properties of the Wiegand wire are described in Section 2.2.2.

2.1.6 Electromagnetic Induction

Wiegand wires exhibit fast magnetization reversal, which is a unique property of these wires. This magnetization change induces a pulse voltage in the pick-up coil, wound around the wire. This phenomenon of electromagnetic induction from the magnetization reversal is converted to electrical energy. When the current flows through a conducting line, a magnetic field is generated around it. Conversely, when a coil is placed in a magnetic field of time-varying intensity, a voltage is induced in the coil, as shown in Figure 2.9. The voltage and current generated in this phenomenon are called the induced electromotive force and induced current, respectively. By using the following equation, Faraday's law of electromotive induction is described.

$$e = -N\frac{d\phi}{dt} = -\frac{d\Phi}{dt} \tag{2.6}$$

$$\Phi = N\phi \tag{2.7}$$

where e, ϕ, Φ, and N are the induced electromotive force (V), magnetic flux (Wb), interlinkage magnetic flux (Wb), and number of coil turns, respectively. The direction of the electromotive force cancels the change in magnetic flux with time, or follows the right-handed screw rule.

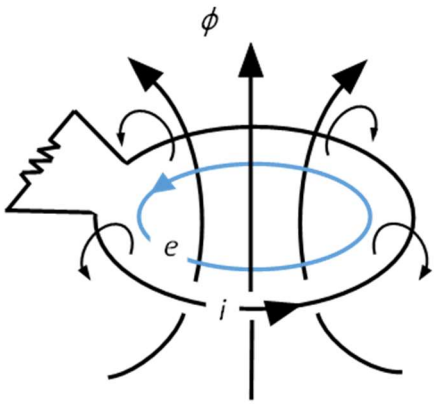

Figure 2.9 Faraday's law of electromagnetic induction.

2.2 Wiegand Sensor

2.2.1 Wiegand Effect

In this study, the Wiegand sensor comprises a Wiegand wire and pick-up coil, wound around the wire. The Wiegand wire was invented by Wiegand in 1974.[29] A specific feature of this invention is the fast magnetization reversal in the hysteresis curve of the wire, which is called the Wiegand effect.[30, 31] Wiegand sensors exhibit unique and excellent characteristics compared to other magnetic sensors, such as Hall sensors using the Hall effect and magnetoresistive (MR) sensor using the magnetoresistance effect.[32, 33] The most notable feature of the Wiegand sensor is its output voltage, i.e., the amplitude of the output pulse does not depend on the frequency of the applied magnetic field.[34] Owing to this advantage, the Wiegand sensor has been used to detect movements including rotation. Additionally, it does not require an external power source, and has recently been used in battery-less rotary encoders.[35]

The material used for yielding the Wiegand effect was an FeNi Permalloy alloy. Its magnetic wire exhibits high permeability and low magnetic anisotropy.[29] When this ferromagnetic wire is repeatedly twisted and heat-treated, the inner core of the wire exhibits a smaller magnetic coercivity (soft core); conversely, the outer shell indicates high magnetic coercivity (hard shell). The cross-sectional views of the wire's magnetic structure are shown in Figure 2.10. The magnetization directions of the soft core and hard shell are parallel to each other under an applied magnetic field of a certain intensity along the longitudinal direction, as shown in Figure 2.10 (a). When the applied field is removed, the magnetization of the soft core is reversed by the demagnetizing field in the wire. Under these conditions, the magnetization directions are in an antiparallel configuration, and the wire is magnetically stable in the closed flux of the soft core and hard shell.

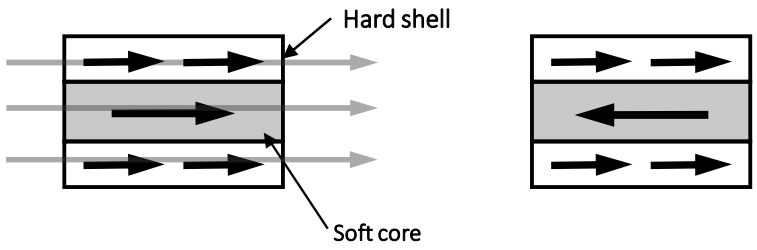

(a) Parallel state (b) Antiparallel state

Figure 2.10 Magnetic structure of the FeNi wire exhibiting Wiegand effect.

2.2.2 Magnetic Structure of the Wiegand Wire

When a stress is applied to a magnetic material, its magnetic properties change. The Wiegand wires are prepared using a heat treatment and twisting process. The atomic composition of the Wiegand wire used herein is 40 wt% Fe–50Co–10V, which is called the Vicalloy. After the annealing and twisting processes, the coercive force near the surface of the wire is reduced. The Wiegand wire has a surface layer that is magnetically soft and a center core that remains magnetically hard.[36, 37] This two-layer structure with different coercive forces is shown in Figure 2.11. In a simple description of the magnetic structure of the wire, the coercive fields of the soft layer and hard core are approximately $\mu_0 H$= 2 mT (H= 1.6 kA/m) and 8 mT (6.4 kA/m), respectively. However, the actual distribution of the coercive force of the wire gradually changes along the radial direction, as shown in Figure 2.11.

In this research, we used a Wiegand wire with a diameter of 0.25 mm and length of 11–13 mm. An alternating magnetic field of $\mu_0 H$= 4–8 mT was applied to the Wiegand wire, and only the soft layer was reversed. This magnetization reversal is accompanied by a large Barkhausen jump in the Wiegand effect.

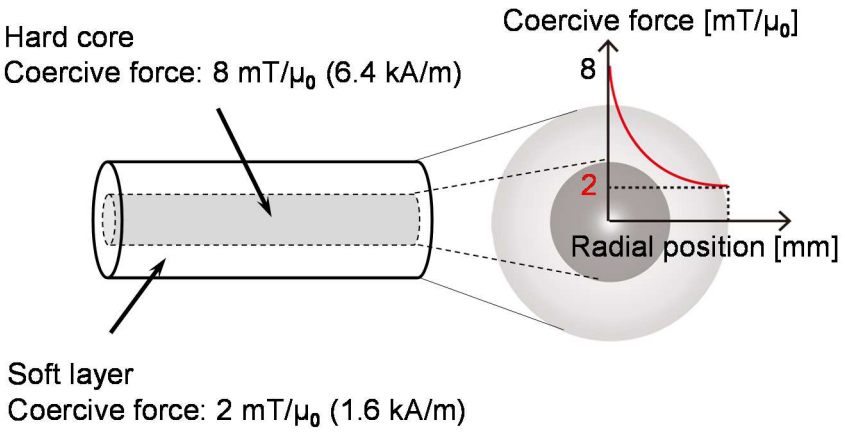

Figure 2.11 Coercive force distribution of the Wiegand wire.

2.2.3 Large Barkhausen Jump

Inside the ferromagnetic material, the magnetic moments are aligned to a certain extent. A region where the magnetic moments are aligned in the same direction is called the magnetic domain structure, as described in Section 2.1.2. The magnetic domain is spontaneously formed, such that the sum of the energies of the magnetic moment is minimized. Simultaneously, the magnetic energy inside the magnetic material does not principally depend on the location, but on defects (such as impurities and grain boundaries) that occur locally owing to stress and other factors that are attributed to a disorderly manner. When a magnetic field is applied, the domain wall does not move smoothly, and collides with these defects. The movement of the domain wall is discontinuous, and this discontinuity can be understood by introducing the change in magnetic energy with peaks and valleys at each position of the defects and irregularities. This discontinuous movement of the domain wall movement is called the Barkhausen effect. When the magnetization curve is traced or the induced voltage is measured during the magnetization reversal, the discontinuous movement of the domain wall, resulting in a discontinuous magnetization change, is observed as a jump in the magnetization curve and noise in the voltage waveform. Therefore, the observed discontinuous magnetization change, due to defects and irregularities in the magnetic materials, is called the Barkhausen jump or Barkhausen noise.

In contrast, the magnetization reversal of the soft layer of the Wiegand wire results in the domain wall moving rapidly and smoothly, without any discontinuity. This specific feature of the magnetization reversal can be confirmed by the steep change in the magnetization curve and the induced pulse voltage to the pick-up coil wound around the wire. These specific features are significantly related to the Wiegand wire and its applications in this study, and are described in detail in the next section. This fast magnetization is called the large Barkhausen effect, and the magnetization change is called the large Barkhausen jump.[38, 39] As described in Section 2.2.1, the material yielding this large Barkhausen jump was introduced by John R. Wiegand, and the fast magnetization reversal typically observed in magnetic wires is called the Wiegand effect. A magnetic wire comprising a Vicalloy of FeCoV, which is known as a typical material yielding the Wiegand effect, is called a Wiegand wire. The magnetic sensor, comprising the Wiegand wire and pick-up coil wound around the wire, is called a Wiegand sensor.[40]

2.2.4 Wiegand Pulse

The Wiegand wire has uniaxial anisotropy in the direction of its length. Magnetization has two stable states, i.e., parallel or antiparallel configurations, of the soft layer and hard core in the length direction, as show in Figure 2.12.[41, 42] Figure 2.13 shows the magnetization curve of the wire. This curve is called a minor loop. The applied magnetic field is limited to an intensity that is sufficient to reverse the magnetization of the soft layer, but not sufficient to reverse that of the hard core. Therefore, the magnetization of the wire was not saturated as a complete material. As shown in the figure, the magnetization change, due to the magnetization reversal of the soft layer, is steep. When an alternating magnetic field of positive and negative fields of this intensity range is applied, the magnetization of the soft layer is reversed repeatedly. This reversal was observed when the intensity of the applied field was approximately 2 mT. As the magnetization of the hard core was not reversed, the configuration of the magnetization of the soft layer and hard core was either parallel or antiparallel. When the initial state of the magnetization is assumed as shown in (A) of Figure 2.13, the magnetization of the soft layer and hard core are aligned in the same direction in a parallel manner. When a magnetic field in the negative direction is applied, the magnetization of the soft layer is reversed at $\mu_0 H = -2$ mT. The magnetizations are antiparallel to each other in the (B) state. With a decrease in the magnetic field (for example, down to $\mu_0 H = -8$ mT), the hard core with a lower coercive force is reversed ((C) state). Although this understanding is somewhat contradictory to the hard core's coercive force of 8 mT, it is actually possible because the coercive force of the wire gradually changes along the radial direction of the wire, as shown in Figure 2.11. In (A), (C), and (D), the soft layer is reversed at $\mu_0 H = 2$ mT. The magnetization of the hard core remains in the same direction altogether, but is partially reversed.

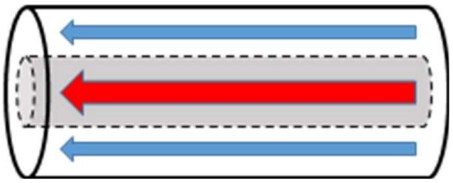

(a) Parallel state

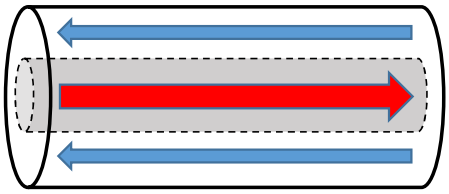

(b) Antiparallel state

Figure 2.12 Magnetization states of the Wiegand wire.

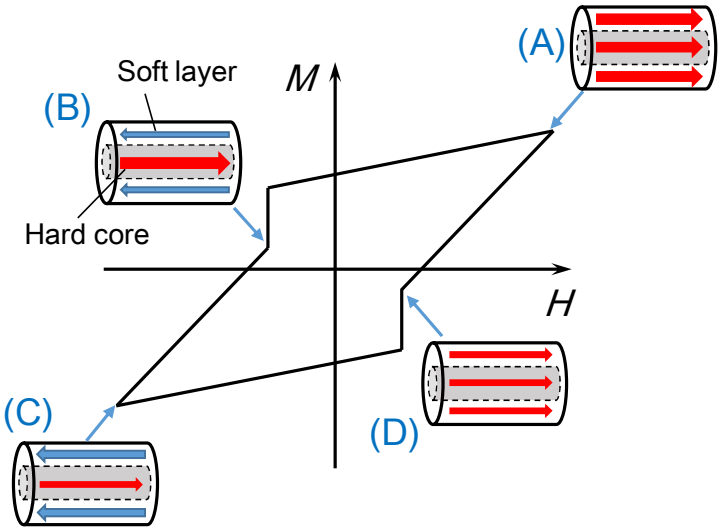

Figure 2.13 Magnetization curve of the Wiegand wire.

A change in the magnetic flux density during magnetization reversal induces a pulse voltage to a pick-up coil wound around the wire. This is the induced electromotive force, which is shown in Equation (2.6). Regarding the specific case using the Wiegand wire,

this pulse voltage is called a Wiegand pulse. Figure 2.14 shows an example of the observed waveform of the Wiegand pulse. Normally, the induced electromotive force voltage, which can be obtained using Equation (2.6) according to the law of electromagnetic induction, is proportional to the rate of change of the magnetic field. However, in the case of the Wiegand effect, the change rate of the magnetic flux density in the Wiegand wire is independent of the change in the externally applied magnetic field. Normally, the magnetization is reversed according to the intensity of the applied magnetic field. For the Wiegand wire, the magnetization reversal of the soft layer is initiated and completed when the intensity of the applied field reaches 2 mT. Therefore, the change in magnetic flux density in the wire is fast. The duration of the magnetization reversal of the soft layer (dt), obtained using Equation 2.6, is determined by the domain wall velocity (v). The velocity is expressed as follows.

$$v = \frac{2J_s(H_w - H_c)}{\beta} \tag{2.8}$$

where J_s is the saturation magnetization, H_w is the magnetic field generated by the reverse magnetic domain, H_c is the magnetic domain wall coercivity, and β is the braking coefficient. A velocity of 500 m/s was reported as an experimentally measured value for the Wiegand wire.[43] The voltage of the Wiegand pulse is proportional to the domain wall velocity, and does not depend on the frequency (change rate) of the applied magnetic field. This specific feature of the Wiegand wire cannot be achieved using other magnetic materials. The Wiegand sensor generates a pulse voltage of constant intensity and pulse width, even when the change in the applied magnetic field is as low as almost zero.

Figure 2.14 shows the waveform of the measured Wiegand pulse. The magnetic field was applied by moving a piece of magnet at an extremely low speed. Under this condition, the rate of change of the applied field intensity was almost zero.[44] The height of the pulse voltage of the pick-up coil was 0.7–0.8 mV per turn, and the pulse width was approximately 20 μs. Both the pulse height and width were independent of the frequency of the applied field. This is significantly advantageous in the application of the Wiegand sensors for power supply as an energy-harvesting element. The height depends on the intensity of the applied magnetic field, because the region of the reversed magnetization depends on the maximum intensity of the applied field.[45, 46]

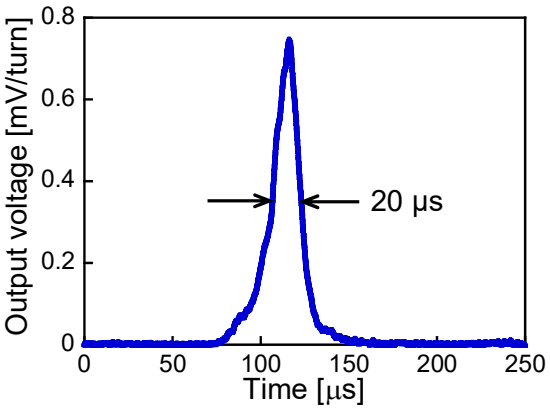

Figure 2.14 Waveform of pulse voltage obtained from the Wiegand wire.

2.3 Electrical Circuit for Wiegand Pulse

2.3.1 Rectifier

By applying an AC magnetic field to the Wiegand sensor, continuous positive and negative voltage pulses were alternately generated. When these voltage pulses are used as a power supply for IoT devices, AC–DC conversion is required. Figure 2.15 shows a block diagram of the AC–DC conversion of the Wiegand pulse. First, a rectifier is used to convert the polarity of the voltage pulse from a negative value to a positive value. Here, half-wave and full-wave rectifier circuits using diodes are introduced, as shown in Figure 2.16. When a forward voltage is applied to the half-wave rectifier circuit, the diode D conducts under forward bias, and the input voltage is applied to the load resistor, R, as shown in Figure 2.16 (a). Conversely, the diode did not conduct under reversed bias. Therefore, only half of the input voltage was applied to the load resistor. In the full-wave rectifier circuit, both the positive and negative voltages can be applied to the load resistance through each of the pathways of two forward-biased diodes. Because the width of the Wiegand pulse is only 20 μs and its single pulse energy is in the order of 1 μw or less,[40] it is necessary to use a full-wave rectifier circuit to obtain the maximum energy.

After the alternating positive and negative voltage pulses are rectified, the pulses are normally smoothed using a capacitor to be used as DC power for electronic devices. The waveform of the smoothed voltage should be stable with fewer ripples. The ripple rate essentially depends on the circuit parameter, which is dominated by the capacitance. DC voltages of 1.8, 3.3, and 5 V are generally used for electronic devices and modules. In practical scenarios, a DC–DC regulator is used. In this study, a self-oscillating boost converter that boosts the DC voltage originating from the Wiegand pulse was developed.

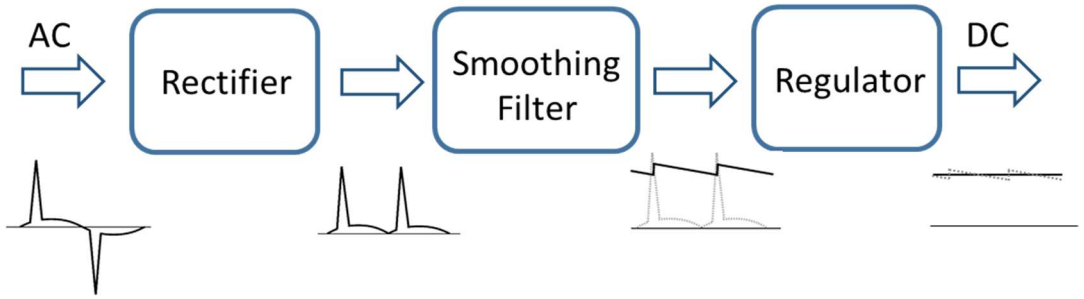

Figure 2.15 Block diagram of an AC-DC signal conversion of the Wiegand pulse.

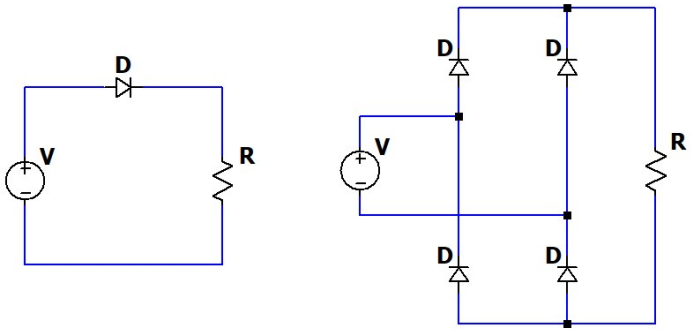

(a) Half-wave rectifier circuit (b) Full-wave rectifier circuit

Figure 2.16 Rectifier circuits using diodes.

2.3.2 Energy Storage Circuit

Energy storage and energy storage circuits are designed for the storage of DC voltage converted from the rectified AC voltage. Capacitors, batteries, fuel cells, and heat engines are commonly used in electronic devices and modules.[47, 48] Li-ion batteries and solar cells are widely used. Furthermore, indoor photovoltaic power generation, piezoelectric power generation, and various low-energy power generation systems have recently attracted considerable attention. Li-ion batteries are widely used energy storage methods; however, they exhibit a short lifespan and decreased energy density. A supercapacitor is also expected to be practically used as a storage device,[49, 50] exhibits the advantage of a fast charging time, and is characterized by a long lifespan and a large discharge current, making it suitable for use as a self-powered power supply. [51]

In this study, an externally applied alternating magnetic field of 1 kHz was used as the excitation source to generate electrical power. A voltage pulse was obtained from the Wiegand sensor excited by the AC magnetic field. The pulse width was quite narrow, and the duty cycle was extremely low. A storage capacitor is necessary to maintain the voltage level as a DC voltage source.

2.3.3 Battery-less Modules

As previously described, battery-less modules and energy-harvesting systems are key technologies for the realization of IoT technology. Here, solar power generation, piezoelectric power generation, and Wiegand sensors as power generation devices are reviewed.[52] The most basic solar cell comprises a p-n junction of a semiconductor. When it is exposed to photon radiations of energy larger than the bandgap of the semiconductor, a voltage is induced across the p- and n-type layers. The open-circuit voltage of a single solar cell is approximately 0.8 V. Therefore, the solar cells are connected in series to obtain a high voltage. Their parallel connection was also used to increase the current flow. A combination of the solar cell generator and Li-ion power storage system can reduce the efficiency of energy storage, depending on the sunlight intensity.[53, 54]

Piezoelectric energy is generated owing to the piezoelectric effect observed in dielectric materials. When the piezoelectric material, which yields piezoelectric properties, is subjected to an externally applied pressure or mechanical stress, polarization is induced in the material. This polarization is accompanied by an electric field, which is derived as the voltage. When vibrating mechanical stress is applied to the piezoelectric material, an alternating voltage is generated. Therefore, this piezoelectric power generation converts vibration energy into electrical energy. The energy density of the piezoelectric power generator is relatively high. It can produce a large output power even with a small vibration. This is because the vibration of a small amplitude deforms the piezoelectric material if suitably designed, e.g., a cantilever structure.[55-57] The piezoelectric power generator can be fabricated in miniaturization and integration occasions and is suitable for energy harvesting and power supply for self-powered devices.

The Wiegand sensor used in this study generates a voltage pulse. The most attractive feature of this sensor used as a power generator is that the pulse voltage does not depend on the frequency or changing rate of the applied magnetic field. When a magnetic field is applied using a tiny piece of a permanent magnet, the Wiegand sensor generates a voltage pulse of constant amplitude and width independent of the speed of the movement of the magnet.[58] This feature cannot be achieved by any other power generator using electromagnetic induction or other power generators. The Wiegand sensor is a promising device for practical application in energy-harvesting and self-powered electronic modules.

Chapter 3: Circuit Model for Wiegand Sensor

This chapter is one of the two chapters describing the research results of the main contribution of this thesis. It is important to develop optimum electrical circuits for the Wiegand sensor. The design and verification of fundamental circuits comprising a rectifier, smoothing, and load resistance are described in this chapter. To evaluate the circuits, an equivalent circuit model of the Wiegand sensor is proposed. Using this equivalent model, it is possible to calculate the circuit performance connected to the Wiegand sensor using a versatile simulation tool widely used for circuit simulation.

3.1 Open Circuit Voltage of Wigand Sensor

In this research, a twisted magnetic wire composed of $Fe_{0.4}Co_{0.5}V_{0.1}$ was used,[59] with its length and diameter as 11 mm and 0.25 mm, respectively. The wire has a two-layer magnetic structure, as illustrated in Figure 2.11. The outer layer and inner core exhibit magnetically soft and hard properties with their coercive forces at 1.6 kA/m and 6.4 kA/m, respectively. In order to achieve this specific magnetic property of the wire, annealing and torsion stress are applied to the wire. The magnetic properties of twisted FeCoV wires depending on the conditions of annealing and torsion stress have been previously reported in detail.[60, 61] A torsion stress is first applied to the wire during its preparation. After the stress is released, the outer layer near the surface becomes magnetically soft, and the inner core remains magnetically hard.[62] The wire exhibits a uniaxial magnetic anisotropy in the longitudinal direction.[63] Because of this magnetic structure, magnetizations of the two layers are parallel or antiparallel to each other, depending on the intensity of the applied external magnetic field H_{ex}. The details of the magnetization reversals of the Wiegand wire is described in Section 2.2.4.

When the magnetization of the soft layer was reversed, accompanied with a large Barkhausen jump, the pulse voltage was induced in the pick-up coil, as shown in Figure 3.1. After this abrupt change in magnetization of the soft layer from parallel to antiparallel states to that of the hard core as shown in Figure 2.12, the magnetostatic energy of the wire is reduced. The number of turns of the coil used in this study was 3000. The peak voltage was 2.5–3.0 mV per one turn of the pick-up coil. The domain wall in the FeCoV wire was reported to be moving at approximately 500 m/s, which is independent of the

change rate of the applied field intensity.[43] Owing to this fast movement of the domain, the full width of the induced pulse was approximately 20 μs.

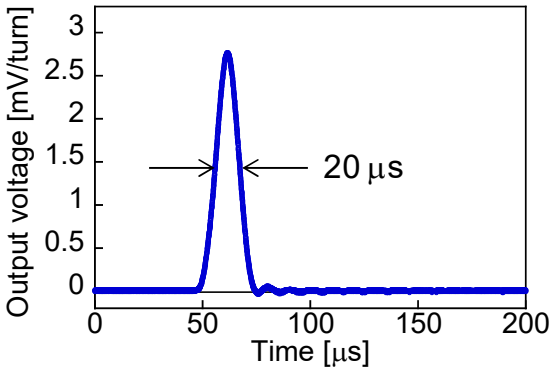

Figure 3.1 Example of a waveform of pulse voltage obtained from the Wiegand sensor.

3.2 Output Characteristics of Wiegand Sensor

The output voltage shown in Figure 3.1 is the open-circuit voltage, V_{open}, induced across both the ends of the pick-up coil, as shown in Figure 3.2 (a). In practical applications, the Wiegand sensor is connected to a load or other electrical circuits. The output voltage, V_{out}, across the load resistance indicated in Figure 3.2 (b) was measured. An alternating magnetic field of 3.2 kA/m in amplitude and at a frequency of 1 kHz was applied to the wire in order to switch the soft layer of the wire continuously. Figure 3.3 shows the typical waveforms of V_{out}. The load resistance of R = 180 Ω, 500 Ω, or 1 kΩ was connected to the Wiegand sensor. V_{out} is smaller than V_{open} because of the voltage drop due to the current flow.

In order to evaluate and develop the electrical circuits used in applications of the Wiegand sensor, an equivalent circuit model is proposed in this paper. The Wiegand sensor consisted of a Wiegand wire and a pick-up coil, which are shown in the equivalent electrical circuit in Figure 3.2 (b), where V_{in}, R_w, and L_w are the intrinsic pulse voltage as the power source, internal resistance, and internal inductance of the pick-up coil in the Wiegand sensor, respectively. The output pulse voltage depending on the load resistance, R, can be explained by the equivalent electrical circuit shown in Figure 3.2 (b).

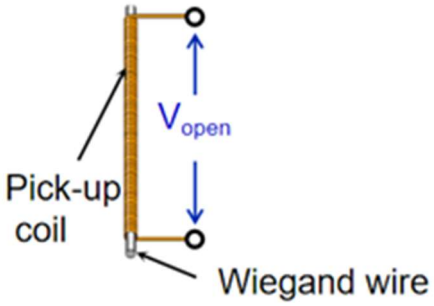

(a) Open-circuit voltage, V_{open} of the Wiegand sensor

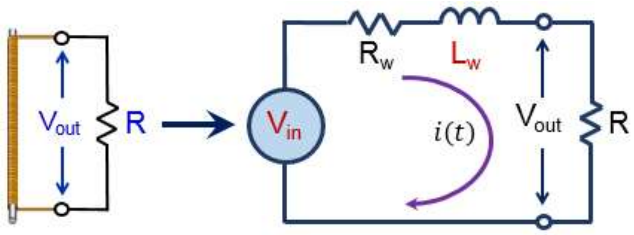

(b) Equivalent electrical circuit model of the Wiegand sensor connected with a load resistance.

Figure 3.2 (a) Open-circuit voltage and (b) equivalent electrical circuit model of the Wiegand sensor.

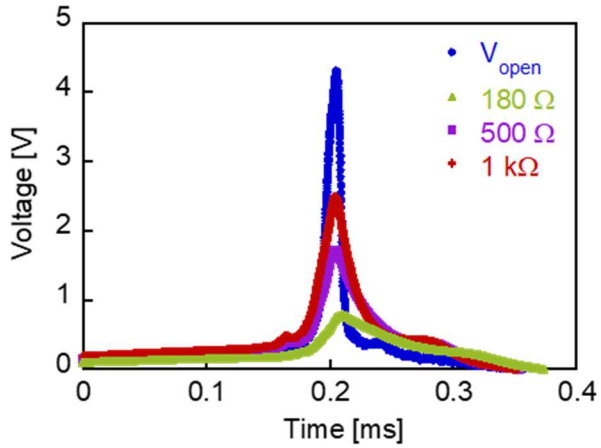

Figure 3.3 Experimentally measured waveforms of the open-circuit voltage and output voltages.

3.3 Equivalent Electrical Circuit for Wiegand Sensor

3.3.1 LCR measurement

The internal resistance, R_w, and inductance, L_w, were measured using a LCR meter (HIOKI IM3536). R_w = 180 Ω was obtained, which agrees with the value determined by the simple current-voltage measurement of the pick-up coil in the Wiegand sensor. L_w = 2.54 mH was obtained by the LCR measurement, but the inductance depends on the magnetization state of the magnetic wire in the sensor.[64] Therefore, it is not appropriate to use the inductance value measured by an LCR meter. In order to evaluate an electrical circuit connected to the Wiegand sensor, the effective value of L_w, which gives the correct circuit simulation, is significant.

3.3.2 MATLAB®/Simulink® Model

In order to determine the effective value of L_w and the time-dependent intrinsic pulse voltage, V_{in}, circuit simulation using MATLAB®/Simulink® was performed. In the circuit shown in Figure 3.2 (b), the following equations are derived:

$$V_{in} = (R + R_w)i(t) + L_w \frac{di(t)}{dt} \tag{3.1}$$

$$V_{out} = i(t)R \tag{3.2}$$

Where i(t) and V_{out} are the current in the circuit and voltage across the load resistance R, respectively. These equations are converted by the Laplace transformation to:

$$V_{out} = \frac{R_w}{L_w\, s + (R + R_w)} V_{in} \tag{3.3}$$

Figure 3.4 shows the block diagram for the electrical circuit model. By using the experimentally measured values of R_w and V_{out}, L_w and V_{in} were determined by simulation. "From Spreadsheet block" gives the input data by referring to the measured waveform of V_{out}, "Gain block" gives the circuit current $i(t)$, and "Derivative block" calculates $di(t)/dt$. After assuming the internal inductance L_w, the intrinsic pulse voltage V_{in} is calculated. By using this simulated result of V_{in} and "Transfer Fcn block" by processing equation 3.3, the waveform of V_{out} is obtained. By fitting the calculated and experimentally measured waveform of V_{out}, L_w and the waveform of V_{in} can be determined.

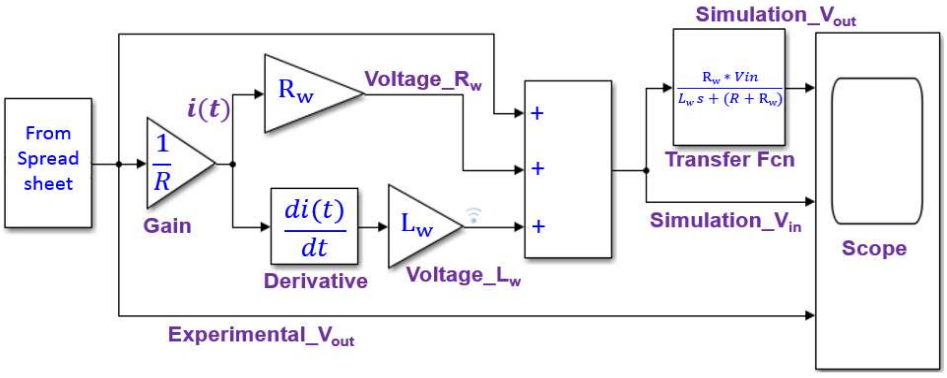

Figure 3.4 Block diagram for simulating the electrical circuit model of the Wiegand sensor by MATLAB®/Simulink®.

3.4 Intrinsic Pulse Voltage of Wiegand Sensor

3.4.1 Effective Inductance of Wiegand Sensor

A method to determine the intrinsic voltage waveform of the Wiegand pulse is described in this section. The output voltage, V_{out}, was experimentally measured prior to any calculation. The intrinsic voltage, V_{in}, was calculated using the Block diagram shown in Figure 3.4. In this calculation, the intrinsic resistance, R_w, and inductance, L_w, of the pick-up coil of the Wiegand sensor had to be appropriately set. As described in the previous section, R_w= 180 Ω was obtained by the current–voltage measurement of the pick-up coil of the Wiegand sensor. Figure 3.5 presents the preliminary calculation results. The calculated V_{in} was dependent on L_w. The load resistance, R, was 1 kΩ. Because the calculated V_{in} had to be constant irrespective of the different values of R, V_{in} was calculated using various combinations of L_w and R.

Next, the optimization of L_w is described. Figure 3.6 shows the dependency of calculated V_{in} on L_w. The load resistances, R, were (a) 180 Ω, (b) 1 kΩ, and (c) 10 kΩ. Herein, the calculated V_{in} was considered to be independent of R under an optimized value of L_w. As shown in Figure 3.6, similar waveforms of V_{in} were obtained when L_w = 15 mH and 20 mH. Therefore, V_{in} was calculated in detail using L_w in the range of 15 mH and 20 mH. Figure 3.7 shows the calculated V_{in} for each case of L_w = 16, 17, 18, or 19 mH. The load resistance was 180 Ω or 1 kΩ. Notably, the waveforms of V_{in} were almost similar in the examined range of L_w.

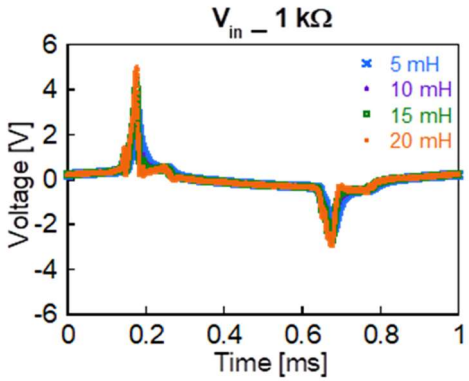

Figure 3.5 Calculated intrinsic pulse voltage, V_{in} depending on the internal inductance L_w of the Wiegand sensor. The load resistance R is 1 kΩ.

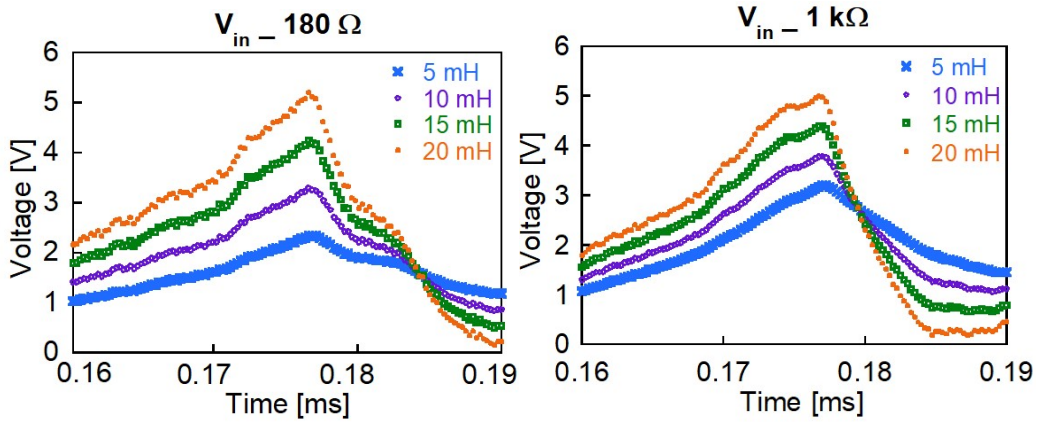

(a) Load resistance R= 180 Ω (b) Load resistance R= 1 kΩ

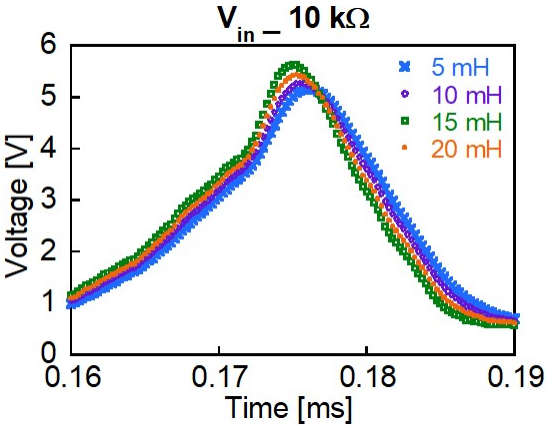

(c) Load resistance R= 10 kΩ

Figure 3.6 Calculated intrinsic pulse voltage, V_{in} depending on the internal inductance L_w of the Wiegand sensor. The load resistance R is (a) 180 Ω, (b) 1 kΩ , and (c) 10 kΩ, respectively.

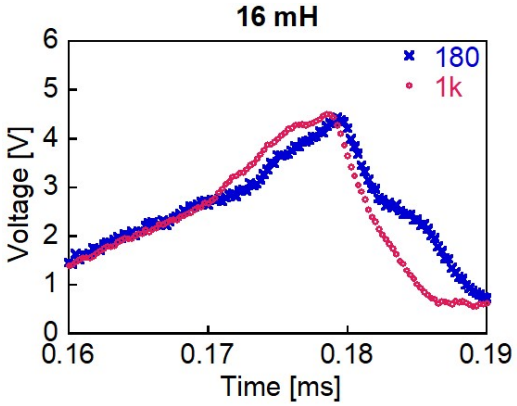

(a) Internal inductances L_w= 16 mH

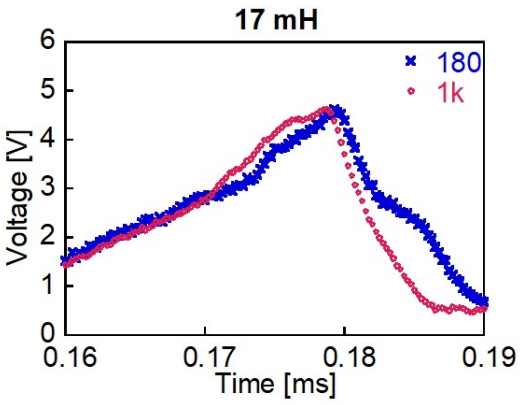

(b) Internal inductances L_w= 17 mH

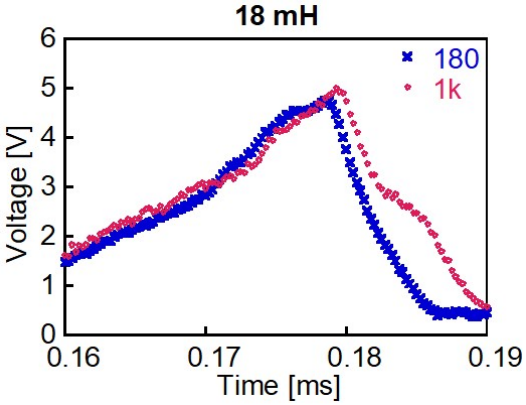

(c) Internal inductances L_w= 18 mH

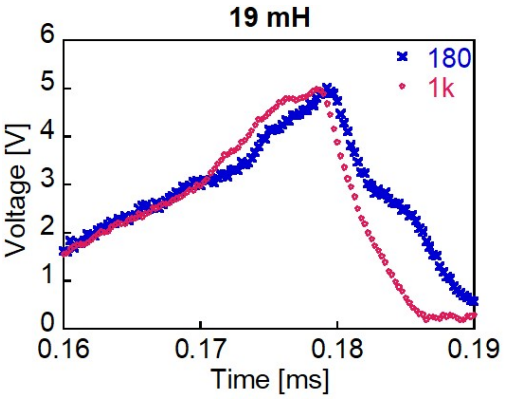

(d) Internal inductances L_w= 18 mH

Figure 3.7 The different value of internal inductances L_w of the Wiegand sensor intrinsic pulse voltages V_{in} under the load resistance 180 Ω and 1 kΩ.

Figure 3.8 shows the peak values of the intrinsic pulse voltage V_{in}, calculated as functions of the internal inductance, L_w The load resistance used was either R= 180 Ω or R = 1 kΩ. Ideally, V_{in} should be constant and independent of R; thus, we chose the inductance value at which the intrinsic pulse voltage was most similar for the two load resistances. From the figure, L_w is thus determined to be 17 mH. This is an effective value of the inductance for circuit response

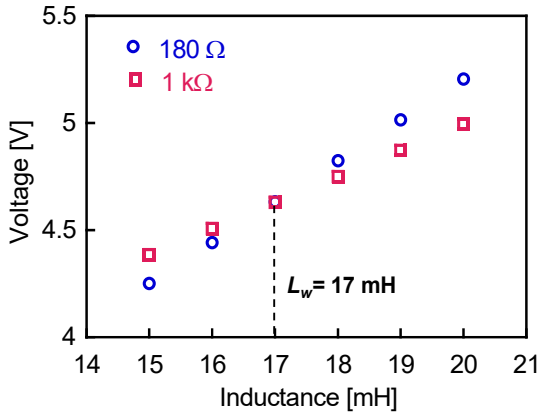

Figure 3.8 Peak values of intrinsic pulse voltage, V_{in}, as functions of internal inductances. The load resistor R is either 180 Ω or 1 kΩ.

The equivalent circuit model of the Wiegand sensor was successfully determined. This is significant because the experimentally measured open-circuit voltage from the sensor is not useful for circuit simulation. A waveform of the intrinsic voltage was proposed in this study. This intrinsic voltage was derived using the experimentally measured internal resistance and optimized internal inductance. In addition, K. Takahashi *et al.* reported that the inductance of the Wiegand sensor under an applied alternating magnetic field is time dependent.[65] Figure 3.9 illustrates the measured inductance of the Wiegand wire during one cycle of the applied alternating magnetic field at 1 kHz. The magnetization of the Wiegand wire was reversed when the intensity of the applied field reached the switching field of the wire. The inductance of the pick-up coil in the Wiegand sensor was affected by the magnetization states, including the direction of magnetization. Therefore, the internal inductance of the Wiegand sensor was changed during its operation. Nevertheless, a constant inductance value is required and is useful in circuit simulation.

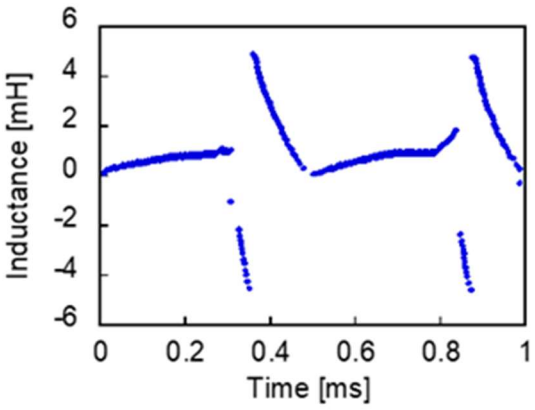

Figure 3.9 Measured inductance of the Wiegand wire during one cycle of the applied alternating magnetic field at 1 kHz.[65]

3.4.2 Optimized Equivalent Circuit Model and Intrinsic Pulse Voltage

Figure 3.10 shows the waveforms of the calculated V_{in}, V_{out}, and experimentally measured V_{out} (L_w = 17 mH and R = 500 Ω). The calculated and measured waveforms of V_{out} agree with each other, and the simulation is thus accurately processed. The waveform of the intrinsic pulse voltage of the Wiegand sensor, V_{in}, is therefore noted to be correctly determined with the abovementioned component values. The peak value of V_{in} for the pick-up coil of 3000 turn is 4.62 V.

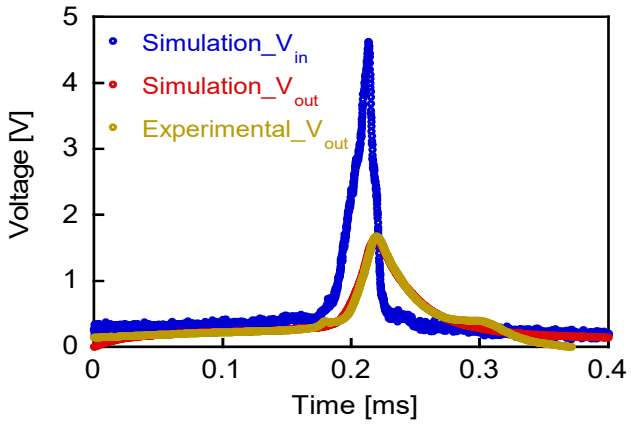

Figure 3.10 Waveforms of calculated V_{in}, V_{out}, and experimentally measured V_{out}.

3.5 Verification of Equivalent Circuit Model

3.5.1 Full-wave Bridges Rectifier Circuit

In the practical application of the energy harvester source such as Wiegand sensor for power generation and energy harvesting, a bridge rectifier circuit is normally used.[66-69] The rectifier circuit prevents the backflow current to the Wiegand sensor, which is a conductive element composed of the inductor and resistor as well as a power source. The circuit response of the Wiegand sensor connected through a full-wave bridge rectifier circuit was studied.[64] We measured the output voltage across the load resistor through a full-wave bridge rectifier circuit connected with the Wiegand sensor, and also calculated the voltage using LTspice®. As shown in Figure 3.11, the Wiegand sensor as a power source is expressed by V_{in}, R_w, and L_w, which are determined by the MATLAB®/Simulink® simulation. When we apply an alternating magnetic field to the Wiegand sensor, the magnetization of the magnetic wire is switched to positive and negative directions in one cycle of the applied field, resulting in positive and negative output pulse voltages. Therefore, $+V_{in}$ and $-V_{in}$ are used as input voltages to the full-wave bridge rectifier circuit. As a rectifying diode for the bridge circuit, a Schottky barrier diode, RBR3MM30A,[70] which is commercially supplied by ROHM, was used. It is indicated as "RBR3MM30A" in the figure, and "R3" in the figure is the load resistor.

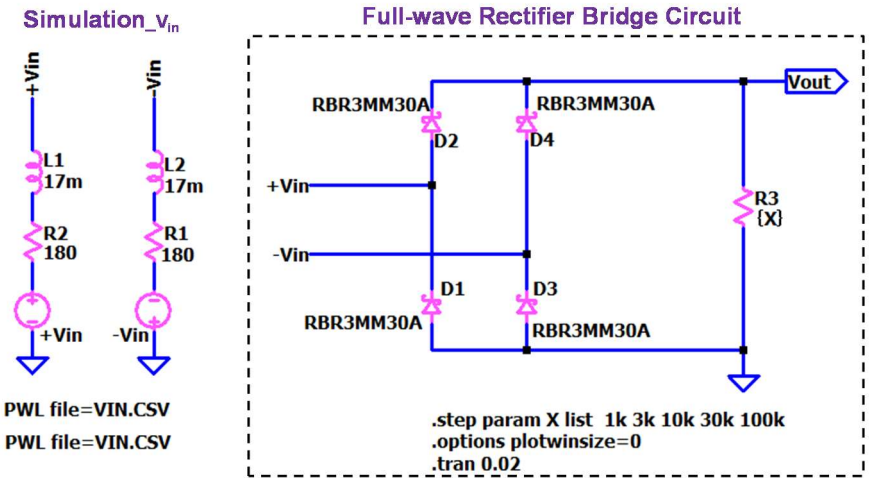

Figure 3.11 Simulation of full-wave bridge rectifier circuit connected to the Wiegand sensor by LTspice®.

3.5.2 Simulated and Experimental Voltages of Wiegand Sensor

Figure 3.12 shows the waveforms of the experimentally measured output voltage, V_{out}. The load resistance R = 1, 3, 10, 30, or 100 kΩ. In the experiment, the waveforms are superimposed with several additional pulse signals, which are possibly resonant signals due to the inductance of the Wiegand sensor and the internal capacitances of the Schottky barrier diodes.

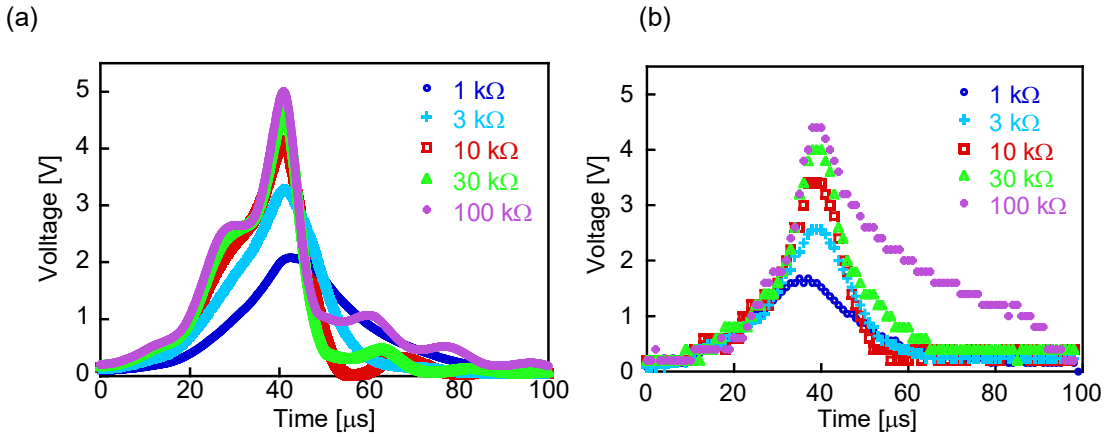

Figure 3.12 Waveforms of (a) experimentally measured and (b) calculated output voltage, V_{out}, across the load resistor. Load resistance R= 1, 3, 10, 30, and 100 kΩ.

The upper graph of Figure 3.13 shows the waveform of the intrinsic pulse voltage, V_{in} as the power source of the Wiegand sensor calculated using MATLAB®/Simulink®. It is assumed that an alternating magnetic field of 3.2 kA/m amplitude and 1 kHz frequency was applied to the circuit. As the magnetization of the soft layer switches along both directions of the wire, alternating positive and negative pulses of period 1 ms are observed. The bottom graph of Figure 3.13 shows the waveform of the output voltage across the load resistor of 10 kΩ, V_{out}, calculated using LTspice®. Figure 3.12 shows the waveforms of the calculated output voltage, V_{out}, across the load resistor, R. The experimental and calculated waveforms shown in Figures 3.12 (a) and 3.12 (b) are observed to be similar, implying that whole process of the simulation including determination of V_{in} and L_w is appropriate.

The optimized value of L_w = 17 mH is quite differenct from 2.54 mH obtained by the LCR measurement; however, it is useful as the effective inductance for reproducing the experimental results by circuit simulation. The calculated waveforms do not exhibit superimposed additional pulse signals because the LTspice® simulation does not consider the internal capacitances of the Schottky barrier diodes. In the simulation, the power loss at the bridge rectifier circuit is considered, which is 26 nJ for a single Wiegand pulse. Although this loss is an unignorable amount compared to the power consumption at the load resistor of 57 nJ, the rectifying circuit is necessary in order to prevent the backflow current to the Wiegand sensor, as discussed in Section 3.6.

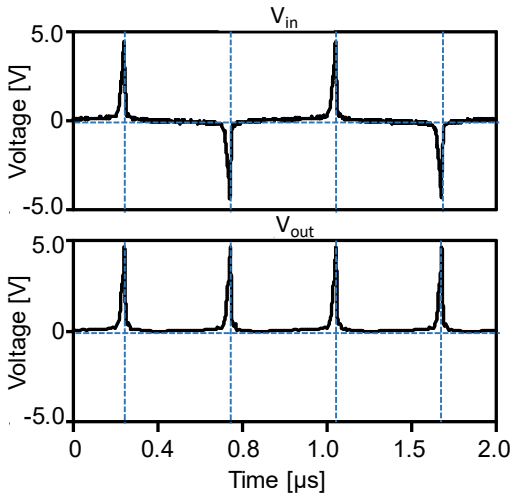

Figure 3.13 Waveforms of intrinsic pulse voltage, V_{in}, from the Wiegand sensor calculated using MATLAB®/Simulink® (top), and output voltage across load resistor R=10 kΩ, V_{out}, calculated using LTspice® (bottom).

Figure 3.14 shows the peak values of the experimentally measured and calculated output pulse voltages plotted as functions of the load resistances. In the calculation, V_{in}, derived using MATLAB®/Simulink® with the considered R_w and L_w, is used as the power source of the Wiegand sensor. Their dependences on R are quite similar. The reason for the difference of ~0.5 V between the experiment and simulation results is not clear. Even with this difference, simulations that use the open-circuit voltage, V_{open}, cannot reproduce the experimental results. We can thus successfully demonstrate the effectiveness of introducing the intrinsic pulse voltage, V_{in}, as well as internal resistance and inductance of the Wiegand sensor. These circuit parameters were derived from the experimental results measured at room temperature. Both the open-circuit an intrinsic voltages are dependent on the temperature because the magnetization of the wire reduces with

increasing temperature. The inductance L_w is also dependent on the magnetization. In case of simulating a circuit operated at temperatures other than the room temperature, it is necessary to perform another measurement at that temperature and to calculate the circuit parameters.

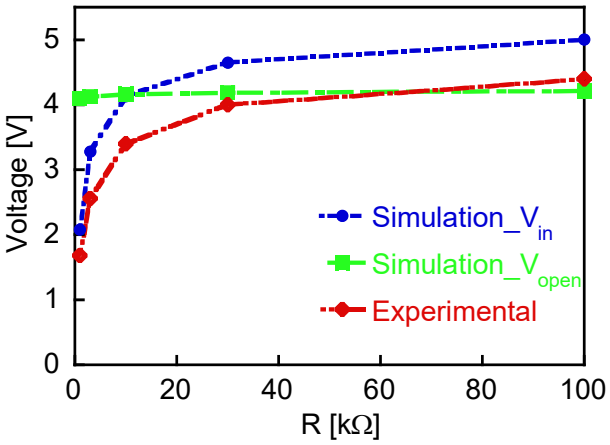

Figure 3.14 Peak values of experimentally measured and calculated output pulse voltages, V_{out}, plotted as functions of load resistance, R. For simulation, (1) V_{in} derived using MATLAB®/Simulink® with considered R_w and L_w, or (2) measured open-voltage, V_{open}, is used as the power source of the Wiegand sensor.

3.6 Summary

In this chapter, the concept of an intrinsic pulse voltage from the Wiegand sensor as its power source is described. Conventionally, the pulse voltage has been discussed as the measured open-circuit voltage across the pick-up coil of the sensor. For analysis of circuit connected to the Wiegand sensor, this open-circuit voltage is not applicable because of the voltage drop due to current flow. Using MATLAB®/Simulink® simulations, we determined the circuit parameters of the internal resistance and inductance of the pick-up coil, and the time-dependent (waveform of the) pulse voltage as the intrinsic pulse voltage. As an example of the circuit simulation, circuit responses through the full-wave bridge rectifier circuit connected to the Wiegand sensor were calculated. The calculated output voltages agree with the experimentally measured values, and the effectiveness of using the intrinsic pulse voltage, and the internal resistance and inductance of the Wiegand sensor, is thus demonstrated.

Chapter 4: Self-Oscillating Boost Converter

This chapter presents the research results regarding the design of a self-oscillating boost converter circuit as well as a quantitative analysis of the power generated by the Wiegand sensor. A stable DC output voltage of 5 V was successfully obtained, which is required for a power source in self-powered devices and battery-less modules. The experimental and calculated results of the voltage/current and ripple characteristics are described in detail. The results of this study suggest the possible use of the Wiegand sensor as a power source for battery-less devices and modules.

4.1 Essentials of Boost Converter

4.1.1 AC–DC Converter

When the Wiegand sensor is excited by an alternating magnetic field, it alternately generates positive and negative voltage pulses.[71] In this study, the AC magnetic field intensity used for excitation was set to 3.2 kA/m, and the excitation frequency was set to 1 kHz. Therefore, it can generate positive and negative pulse voltages with a frequency of 1 kHz, which is regarded as an AC voltage source. If the AC voltage is successfully converted into a DC voltage output, the energy harvesting of the Wiegand sensor will be achieved.

The general AC–DC conversion process is illustrated in Figure 4.1.[72, 73] First, the AC voltage is rectified, then smoothed, and finally connected to a voltage stabilizer, step-down, or step-up circuit according to the required voltage value. In this study, the Wiegand pulse voltage is the AC power input of the AC–DC converter; a rectifier circuit is needed to prevent the current from flowing back to the Wiegand sensor. Therefore, we first need to rectify the Wiegand pulse; the full-wave bridge rectification is described in Section 3.6. The bridge rectifier circuit is advantageous owing to the fact that the maximum reverse voltage of the small signal diode is low, the output voltage is high, and the ripple voltage is small. Moreover, because the source AC voltage provides current to the load during the positive and negative half cycles, the voltage can be fully utilized and the efficiency is high. As shown in Figure 4.2, the output voltage of the rectifier must be smoothed by a filter circuit to obtain a DC voltage. The filter circuit can be an independent capacitor or a combination of inductors, capacitors, and resistors. If the smoothed voltage ripple is excessively large, a voltage regulator must be connected to the filter circuit to

generate a stable voltage. Next, we discuss the DC voltage output in the case of smoothing with capacitors.

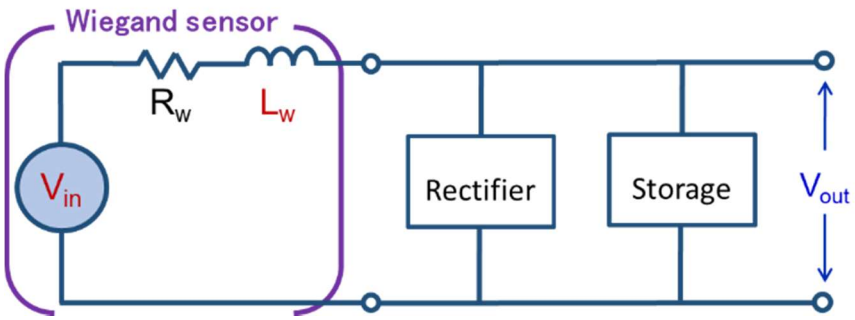

Figure 4.1 AC–DC converter composition of Wiegand sensor.

As shown in Figure 4.2, the Wiegand pulse voltage has no voltage for an extended time within an effective period; therefore, it is particularly important to choose a smoothing capacitor to obtain the highest stable voltage. If the capacitance is too large, the charging time is extended, and the discharge starts when the charging does not reach the peak value. If the capacitance is too small, the charging time is too short, and the discharge of the capacitor is rapid. The ripple of the output DC voltage may be too large; therefore, it is difficult to obtain a stable DC voltage.[74-76] The specific circuit verification results are discussed in the experimental circuit.

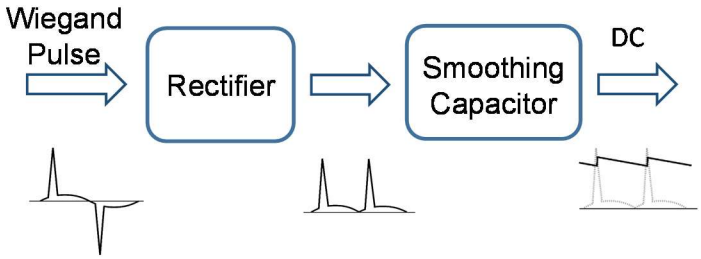

Figure 4.2 Block diagram for the AC–DC conversion of the Wiegand pulse voltage.

4.1.2 DC Conversion of Wiegand Pulse Voltage

The previous section indicated that energy harvesting for Wiegand sensors must first obtain a stable DC voltage. Next, we discuss the output voltage characteristics when a smoothing capacitor is used. In this study, we simulate an AC–DC circuit using LTspice® to compare the actual circuit test to obtain the output voltage characteristics. The circuit is illustrated in Figure 4.2. A smoothing capacitor is placed at each end of the output of the full-wave bridge rectifier and connected to a load in parallel. Therefore, the rectified voltage is an AC voltage, and the DC voltage is obtained through the filter capacitor. In the circuit action process, the smoothing capacitor is charged when the output voltage of the rectifier rises above the voltage of the capacitor. The capacitor provides the required current from the stored charge as the output voltage of the rectifier drops. Therefore, the value of the DC output voltage depends on the value of the smoothing capacitor. Because the output voltage characteristic of the full-wave bridge rectifier circuit of the diode is confirmed in Section 3.5, the description of the line rectifier circuit is omitted here. Owing to the charging and discharging of the capacitor, the smoothing voltage of the capacitor will have different degrees of ripple voltage depending on the value of the capacitor. The ripple rate of the output DC voltage is the main criterion for determining the smoothing effect; we can determine the capacitance value according to the required ripple rate. On the other hand, because the Wiegand pulse wave is characterized by a significantly short pulse width of approximately 20 μs, a suitable smoothing capacitor can extend the power supply time and obtain a stable voltage output.

Owing to the characteristics of the Wiegand pulse, the influence of the capacitance value on the output voltage needs to be verified. Figure 4.3 presents the DC conversion circuit used in this study. The voltage and current of the smoothing capacitor are given by the following equation:

$$V_{C_1} = \frac{I_{C_1}}{C_1} T \tag{4.1}$$

In the ideal steady-state operation of the circuit, C_1 is calculated from the maximum value of the voltage and current. The maximum voltage of V_{in} was 4.62 V, the resistance value of the pure impedance was 180 Ω, and the current value of C_1 was 5.6 mA. The capacitor is charged when the Wiegand pulse voltage occurs. Because the width of the Wiegand pulse is 20 μs, the capacitor can be charged up to 20 μs under ideal conditions. Assuming that the maximum charging time is 20 μs, the smoothing voltage peak value is

proportional to the capacitance, as shown in Formula 4.1. Therefore, the smaller the capacitance value, the higher the voltage peak. The capacitance is inversely proportional to the discharge; however, a smaller capacitance results in a faster charging speed.

Considering that the capacitor can be effectively charged during the Wiegand voltage period, the maximum voltage can be calculated using Formula 4.1. The capacitance value was approximately 24 nF, which was used as the center to investigate the smoothing effect of the capacitor.

To decrease the loss of load resistance, it was fixed at a large resistance of 5.5 MΩ, and the AC–DC conversion was used to obtain a DC voltage from the Wiegand pulse voltage, as shown in Figure 4.3. The DC conversion circuit, diode parameters, capacitors, and resistors were used in our experiments and simulations. C_1 was used in the range of 1–220 nF to analyze a processed and constant DC voltage. C_1 = 1, 10, 20, 50, 100, or 220 nF was connected to the full-wave bridge rectifier, and the waveforms of the output voltage, V_{out}, were measured. Figure 4.4 (a) indicates that V_{out} saturates at 2.77 V regardless of the capacitance of C_1. The relaxation time of the saturation is longer for a smaller C_1. Figure 4.4 (b) presents the simulated waveforms of the output voltage, which agree with the experimental results; to obtain a stable DC voltage, it is not fully charged to the maximum value during the Wiegand pulse period.

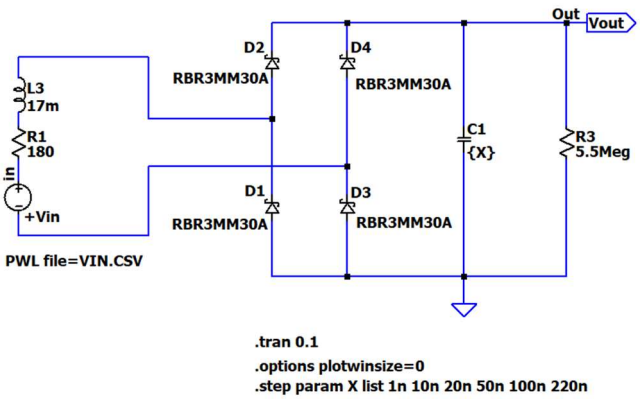

Figure 4.3 DC conversion circuit for the Wiegand pulse voltage.

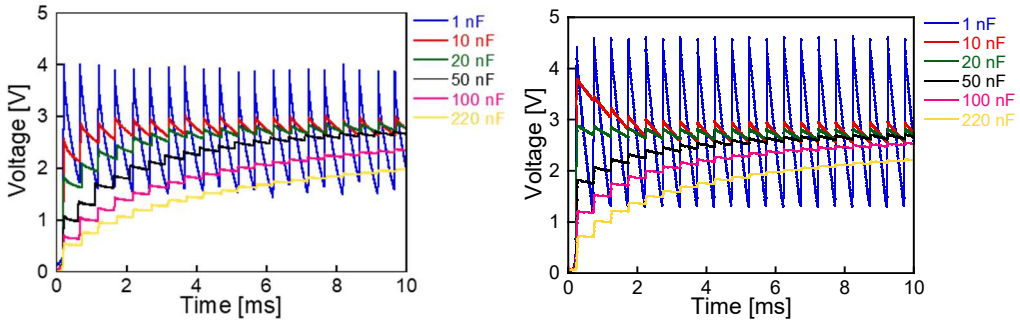

(a) Measured output voltage (b) Simulated output voltage

Figure 4.4 (a) Measured and (b) simulated output voltages after the DC conversion of the Wiegand pulse voltage.

The frequency of the ripple was 2 kHz, which is twice the excitation frequency owing to the full-wave rectifier. The output voltage ripple is high for $C_1 \leq 20$ nF, and it is significantly low for $C_1 > 20$ nF. The ripple rate, *Ripple*, was calculated using the following equation:

$$Ripple = \frac{V_{\max} - V_{\min}}{V_{\text{average}}} \times 100\ [\%] \tag{4.2}$$

where $V_{\max}$, $V_{\min}$, and V_{average} are the maximum, minimum, and average voltages, respectively, applied for 1 ms during one cycle of excitation. The ripple rates calculated from the experimental and simulated output voltages are shown in Figure 4.5.

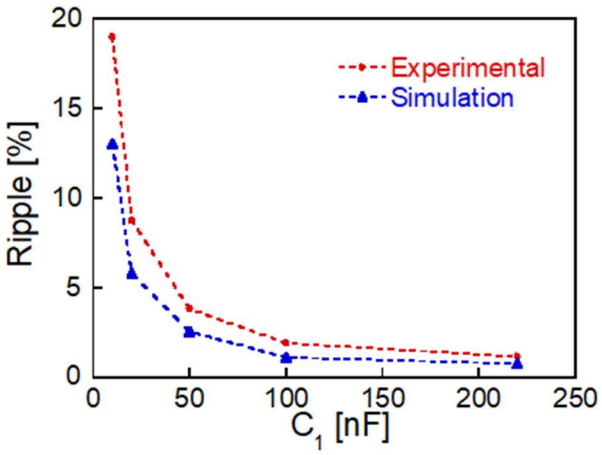

Figure 4.5 Ripple of the output voltage.

The output DC voltage is presented in the subsection above, and the electrical energy U stored in a capacitor can be calculated using the following equation:

$$U = \frac{1}{2} CV^2 \text{ [J]} \tag{4.3}$$

As indicated in Equation 4.3, the electrical energy stored in the capacitor is related to the value of the capacitor and the voltage obtained. When the final voltage is the same, the amount of energy is related to the capacitance. However, the maximum value of energy obtained from the Wiegand pulse in the case of different capacitances can be presented by averaging the generated power. The average power W generated in 1 s can be obtained using Equation 4.4. Here, we know that T is the time at which the power can be stably generated to the highest value when the voltage is DC; therefore, we can calculate the different powers stored when using different capacitors. Figure 4.6 presents the average electrical power of capacitor C_1 at an excitation frequency of 1 kHz. When the capacitance value is 20 nF, the maximum electric power obtained is 15.3 μW. However, the continuous increase in the capacity of the smoothing capacitor requires a longer rise time to reach a stable DC voltage. Therefore, when working with a full-wave bridge rectifier circuit to obtain the maximum energy within the effective time, the capacity of the smoothing capacitor is approximately 20 nF.

$$W = \frac{U}{T}\ [\mathrm{W}] \tag{4.4}$$

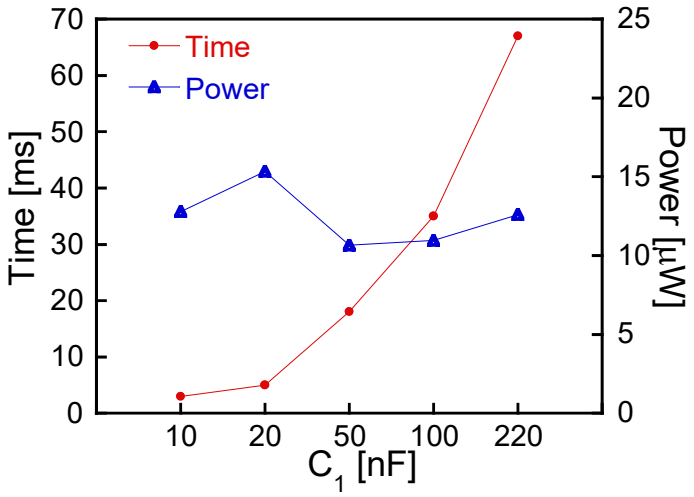

Figure 4.6 Measured harvesting power on capacitor C_1.

For the Wiegand sensor energy harvesting circuit, it is not only necessary to consider whether a stable DC voltage can be obtained after rectification, but also whether it can continue to supply power to the back-end consumer circuit. Therefore, we can consider increasing the capacity of the smoothing capacitor to obtain a more stable output. However, when the charge storage time is longer, the actual startup time of the subsequent circuit will also increase. In case of a power outage, the existing circuit cannot be restarted immediately owing to an extended charge time of the smoothing capacitor; therefore, a Wiegand sensor will need to be utilized to generate electricity, and reducing the startup time needs to be considered. In addition, simply changing the capacitance in the circuit design does not change the response to the load change; a more reliable AC–DC conversion circuit is required. In practical applications, a voltage stabilizer is required to achieve a continuous power supply to the subsequent circuit.[77, 78]

4.1.3 Boost Converter for Wiegand Pulse

For the Wiegand pulse voltage, we obtained a DC voltage output of 2.77 V through rectification and smoothing. Generally, applications related to the Internet of Things require 3.3 V and 5 V to function. Therefore, it is necessary to convert the Wiegand pulse voltage into a DC voltage that can be applied to subsequent electronic devices, such as 3.3 V or 5 V. For a wider range of applications, the purpose of this research is to obtain a stable 5 V output voltage. The peak value of the Wiegand voltage is 4.62 V; it is required to boost the voltage to 5 V. Because an external power supply cannot be used, it is necessary to design the simplest circuit to achieve the boost and reduce its loss for the electronic components. Similarly, the nano-power energy harvesting power supply LTC3588-1 produced by TI can also be used for energy harvesting solutions.[79] LTC3588-1 is an energy harvesting synchronous buck-boost regulator. The working voltage ranges between 2.7–20 V, and the output voltage can be selected as 1.8 V, 2.5 V, 3.3 V, or 3.6 V. Its internal full-wave bridge rectifier rectifies the voltage generated by the piezoelectric vibration and stores the collected energy on an external capacitor. Based on the datasheet of LTC3588-1, it is used for energy sources such as piezoelectric, solar, or magnetic transducers. According to the datasheet, the LTC3588-1 will not work if the voltage between the VIN and GND terminals is less than 5 V. As indicated in Section 4.1.2, the voltage obtained by simple capacitor smoothing cannot reach 5 V.

Next, we will discuss the result of boosting the 2.77 V DC voltage obtained after rectification and smoothing to use the existing boost power of DC–DC LTC3400.[80] LTC3400 is a synchronous, fixed-frequency, step-up DC–DC converter. It starts up at 0.85 V or higher; the 2.77 V output DC voltage of the Wiegand pulse can be used as the input voltage. As shown in Figure 4.7, the simulation electricity obtains a DC voltage of 3.3 V. The applied parameters were obtained from the datasheet of LTC3400. The results are shown in Figure 4.8; when V_{C1} is equal to LTC3400's starting voltage of 0.85 V, the LTC3400 starts to work and the output voltage continuously rises. When the voltage is higher than 3.3 V, it is adjusted by the feedback circuit to make the output a stable 3.3 V. However, there is significant voltage vibration before the voltage reaches stability; therefore, we focus on the treatment before stabilization.

In the case of no load conditions, an output of 5 V is ideal; however, when the load is connected, the DC–DC will consume energy, which will make the output voltage of the Wiegand pulse filter circuit less than the initial voltage of LTC3400. Although the use of existing power ICs can obtain a stable 5 V or 3.3 V DC output from the Wiegand pulse voltage, it may require a long time to obtain a stable output owing to the influence of the

starting voltage. That is, in subsequent circuit applications, a circuit that controls the startup time must be connected, which will increase the loss of the circuit and affect the optimization of energy.

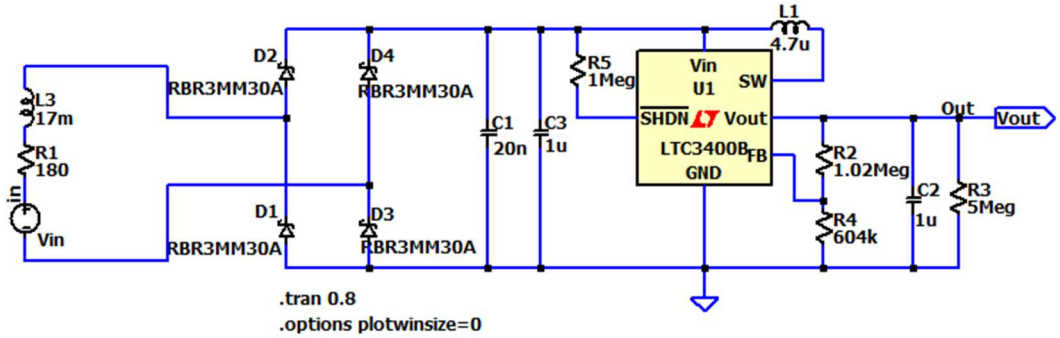

Figure 4.7 Simulated DC voltage 3.3 V circuit of LTC3400.

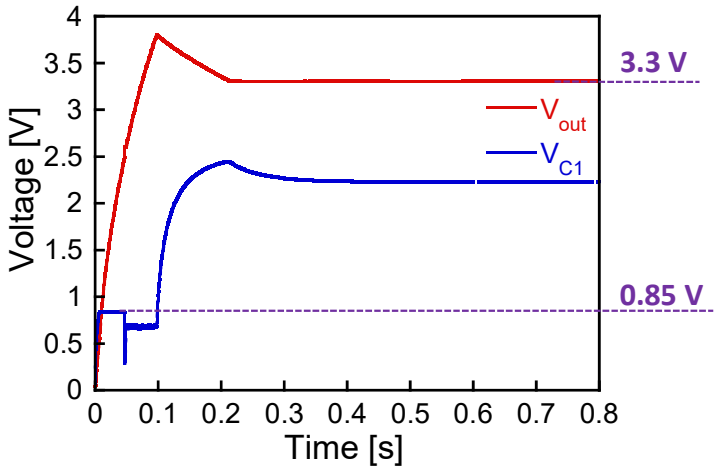

Figure 4.8 Simulated output voltage 3.3 V of LTC3400 circuit.

4.2 Design of Boost Converter Circuit

4.2.1 Principle of Boost Converter Circuit

As indicated in Section 4.1, the maximum voltage that can be obtained through the DC conversion of the rectifier and filter capacitor is 2.77 V. To obtain a voltage of 5 V, a boost converter needs to be used.[81, 82] The booster converter has an inductor on the input side and a current flows from the input to the GND while the switch is on; thus, it is possible to operate despite the input voltage being relatively low. A booster can be used as a power factor correction or force factor improvement circuit (active filter) to suppress harmonic currents.

Figure 4.9 presents the structure of a typical boost converter circuit, where the output voltage must be higher than the input voltage.[83, 84] The principle of the boost converter is to convert the magnetic field energy stored in inductor L into electric field energy. This energy is superimposed with the input power voltage and then filtered by capacitors to obtain a smooth DC voltage. Because this voltage is formed by the superposition of the input power voltage and the magnetic energy of the inductor converted to electrical energy, the output voltage is higher than the input voltage. Thus, the boost process is completed.

First, we describe the operating characteristics of capacitors and inductors in boost converters. The voltage on the capacitor is proportional to the integral of the current. The voltage of the capacitor gradually changes as the current continues to flow. In particular, when a constant current continues to flow, the voltage increases or decreases with a constant slope. In the case of an inductor, the derivative (rate of change) of the current is proportional to the voltage. By applying a continuous voltage, the current gradually increases or decreases with a constant slope. Here, the inductor attempts to pass the current from the higher voltage side to the lower voltage side, similar to the resistor; however, despite the voltage direction being switched, the current direction does not change immediately. Therefore, the voltage flows from the lower voltage side to the higher voltage side transiently.

In the boost converter, the current flows from the input power side through the switch to the inductor while the switch is on. The entire current flows to the GND; thus, the load current is applied by the output capacitor. When the switch is off, the counter electromotive force generated by the inductor causes the diode to turn on, and the current flows from the inductor to the load. This action is suitable for small-current applications.

As shown in Figure 4.9, when SW is switched to 1 pin, inductor L stores the energy from V_{in}; when SW is switched to 2 pin, the energy stored in inductor L is charged to capacitor C. A field-effect transistor (FET) is used instead of SW to constitute a practical application boost converter circuit, as shown in Figure 4.10. In this study, we report a self-oscillating boost converter circuit for a Wiegand pulse voltage. A feature of the booster converter is that the energy stored in an inductor increases the output voltage, which is higher than the input voltage. Figure 4.10 presents the typical circuit of a boost converter. The alternating sequence of storing the energy in the inductor and pulling it back to the circuit boosts the voltage. Generally, the switching ON/OFF of M, a FET controlled by an external signal, is used to apply this alternating sequence. As this study aims to develop self-powered electronic modules, a self-oscillating boost converter is investigated.

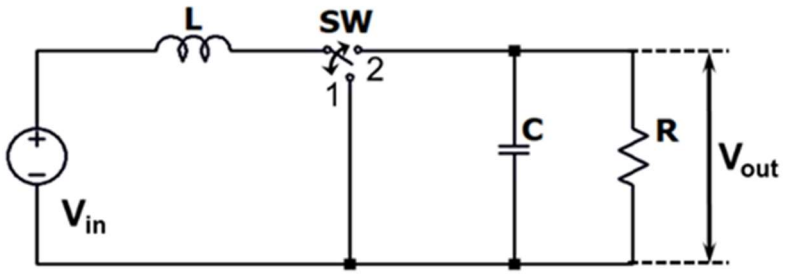

Figure 4.9 Typical boost converter circuit.

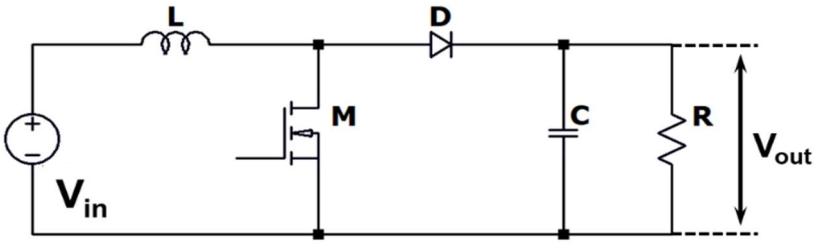

Figure 4.10 Practical application boost converter circuit.

The boost converter consists of two basic distinct states, as shown in Table 4.1.

In the on-state, as shown in Figure 4.11 (a), FET M is ON; as the current I_L flowing through the inductor in the clockwise direction increases, the energy stored in the inductor also increases. Simultaneously, the voltage stored in the capacitor increases.

In the off-state, as shown in Figure 4.11 (b), FET M is OFF; according to Ohm's law, the current decreases as the load increases. Thus, to maintain the current flowing to the load constant, the magnetic field energy generated by the inductor will be consumed more, which indicates that more electricity is obtained to charge the capacitor through diode D, and finally, a higher voltage is obtained.

If the frequency of the control switch is high, the inductor will not be completely discharged. This is because the frequency being too high is equivalent to the switch being always ON, and the voltage on the output side is always higher than that at the voltage source. When the switch is turned on, it charges the capacitor in parallel with the load until the voltage across the capacitor reaches the sum of the voltage stored in the inductor and the power supply voltage. Then, when the switch is turned off, as shown in Figure 4.11 (b), both the left and right circuits are turned on, and the energy stored in the capacitor is released to the resistor. During this period, the diode prevents the capacitor from discharging through the FET. The switch must be rapidly opened again to prevent the capacitor from excessively discharging.

Table 4.1 Two distinct states of boost converter.

	On-State	**Off-State**
M	ON	OFF
D	OFF	ON

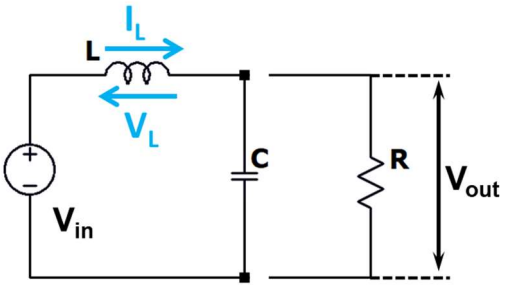

(a) On-State

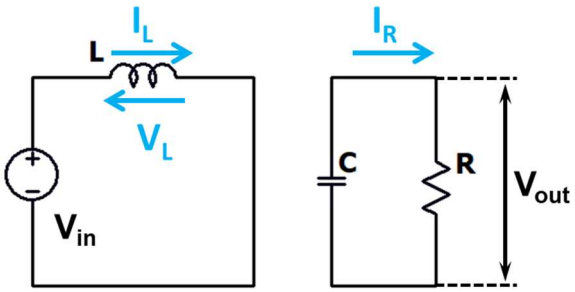

(b) Off-State

Figure 4.11 Two distinct states of boost converter equivalent circuit.

4.2.2 Self-Oscillating Boost Converter

Generally, the ON/OFF ratio of the FET is controlled by square waves.[85, 86] In this research, we aim to design a battery-less boost converter circuit; if the ON/OFF square wave input is used, a waveform generator as an external power to FET ON/OFF is required.[87, 88] Here, the Wiegand pulse voltage can convert FET M to ON; therefore, it is possible for the inductor to store energy. However, the Wiegand pulse voltage width is only 20 μs, indicating that if the FET ON time is less than 20 μs, it will be difficult to achieve the boosting. Figure 4.12 presents the self-oscillating boost converter circuit used in this study for a Wiegand pulse voltage. The input voltage V_{in} of a 20 μs-width pulse used as the power source (see Section 3.5.2) generates an oscillating voltage at V_{C1}. The frequency of these oscillations corresponds to the resonant frequency determined by inductor L_1 and capacitors C_1 and C_{gs}. This oscillation voltage at V_{C1} switches the consecutive ON and OFF states of M, as shown in Figure 4.12.

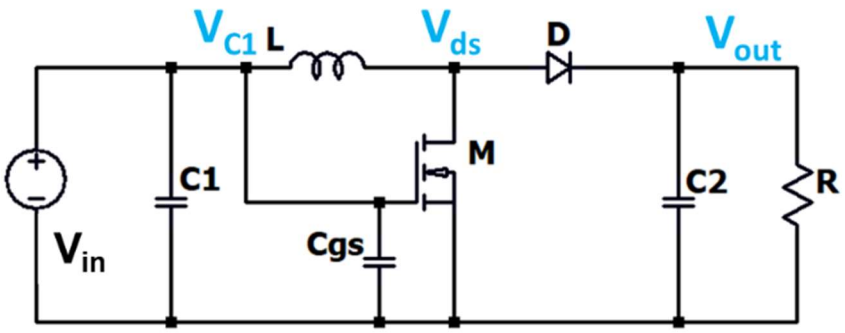

Figure 4.12 Self-oscillating boost converter circuit.

Figure 4.13 presents the typical current and voltage waveforms of the inductor in a self-oscillating boost converter ON/OFF state.

- On-State

When the oscillating pulse voltage V_{C1} is valid above the voltage level at which the FET is turned on, V_{C1} is applied to the left end of the inductor. Then, the FET is turned on and inductor L is connected to GND. Thus, C_1 stores the voltage V_{C1} through the inductor; therefore, the inductor current I_L increases with a constant gradient, as shown in Figure 4.13, and the energy is stored in inductor L.

- Off-State

When the oscillation pulse is below the voltage level at which the FET turns off, the FET is turned off and the energy stored in inductor L is charged to the output side capacitor C_2, and the current I_L also decreases with a constant gradient, as shown in Figure 4.13. The average value does not change from the current waveform of the inductor. A DC output voltage higher than V_{in} is obtained by repeating the switching ON/OFF of the FET. As a result, the aforementioned ON/OFF state operation can be repeated between 20 μs of the Wiegand pulse to achieve a boost. Energy conversion is not performed only once in the 20 μs to maximize the energy of the accumulated pulse voltage.

As shown in Figure 4.13, because a cycle of the inductor current I_{L1} is a triangular wave, it circulates to the ground through capacitor C_1; thus, the voltage V_{C1} of capacitor C_1 also has a triangular ripple voltage. The output voltage at both ends of C_1 provides a constant voltage for the load. When a ripple voltage flows through the load resistance, a ripple current is generated in the resistance, which increases the working current amplitude of the load; thus, the power consumption of the circuit increases. In low-power IoT electronic devices, as the power supply voltage decreases, the requirements for ripple voltage are becoming increasingly stringent. Therefore, the amplitude of the voltage fluctuations must be controlled in the circuit design to reduce circuit loss.

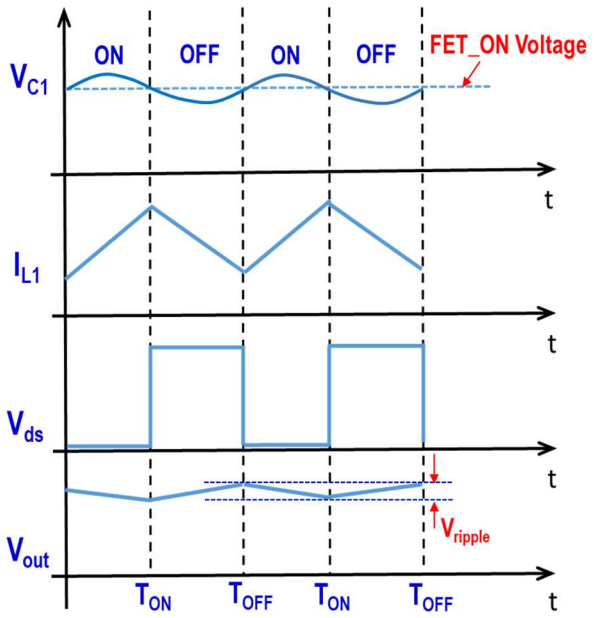

Figure 4.13 Typical waveforms of self-oscillating boost converter.

4.3 Design of Self-Oscillating Boost Converter Circuit

4.3.1 Simulation Circuit

Based on the observations in Section 4.2, the design of the self-oscillating boost converter circuit of the Wiegand pulse is shown in Figure 4.14.

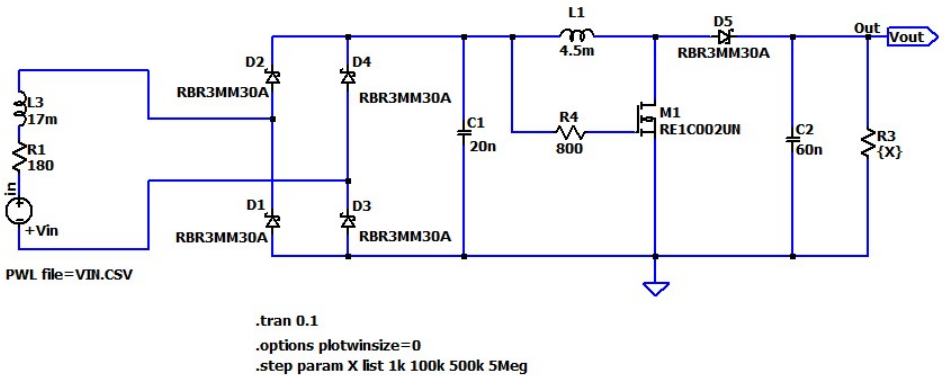

Figure 4.14 Self-oscillating boost converter of the Wiegand pulse.

The parameters of capacitors C_1, C_2, and inductor L_1 are important for designing the self-oscillating boost converter circuit. To obtain an output voltage of 5 V, an LTspice® simulation was used to analyze the optimal parameters. First, for the selection of the FET, we use a small-signal N-channel-type MOSFET that has a low threshold voltage (1.2 V).[89]

Next, we discuss the conditions for the self-oscillation. After the full-wave bridge rectifier, each Wiegand pulse was repeated in 0.5 ms. Namely, the rectified voltage frequency was varied from 1 kHz to 2 kHz. Here, the frequency f_o must be higher than 2 kHz.

Based on the resonance principle, the frequency f_o of the L_1C_1 resonance is determined by the following equation:

$$f_o = 1/\left(2\pi\sqrt{L_1 * (C_1 + C_{gs})}\right) \tag{4.3}$$

As shown in Figure 4.15, the waveform of the boost action is obtained when the output voltage is stable. When FET M_1 is turned OFF, the direction of the current does not change immediately. In certain cases, the inductor current is negative. However, in this boost

circuit, owing to the reverse current prevention effect of diode D_5, it does not cause damage to the circuit. The output voltage can be effectively increased when the input waveform vibrates. For a smoothed voltage of 1.1 V using a self-oscillating boost converter, we can obtain a DC output voltage of 5 V.

Because the FET operating voltage is 0.83 V in the self-oscillating boost converter circuit, according to the datasheet, when V_{ds} is 10 V, the current is 1 mA, and the FET threshold voltage is 0.3 V to 1.0 V; according to the voltage shown in Figure 4.15, when it is turned on at 1.0 V, the current is 20 mA. Furthermore, in this study, we found that when the maximum current is 3 mA and when the voltage is 0.83 V, this fully indicates that the FET is ON.

Comparing the typical waveform shown in Figure 4.13 and based on the enlarged figure shown in Figure 4.16, we can observe that when the input voltage is higher than 0.83 V, the FET is ON, whereby the inductor current increases and energy accumulation is achieved. When the input voltage is lower than 0.83 V, the FET is OFF, and the energy stored in the inductor is transferred to both ends of the capacitor to achieve a boost effect. When the input waveform oscillates, the FET can repeat the ON/OFF cycle to continuously and effectively increase the output voltage.

Figure 4.17 presents the simulated waveforms of the voltages and currents in the self-oscillating boost converter. The rectified voltage of the Wiegand pulse oscillates owing to the resonance of C_1 and L_1. This oscillated voltage V_{C1} switches the FET ON/OFF. V_{ds} confirms the ON/OFF status of the FET. As a result of the oscillated I_{L1} and I_{D5} and the smoothing capacitor C_2, a constant DC voltage is obtained in the output. V_{out} is 5.1 V, which is higher than the input voltage of V_{C1}, and a DC voltage of 2.77 V is obtained without the booster circuit, as shown in Figure 4.4, which is working normally.

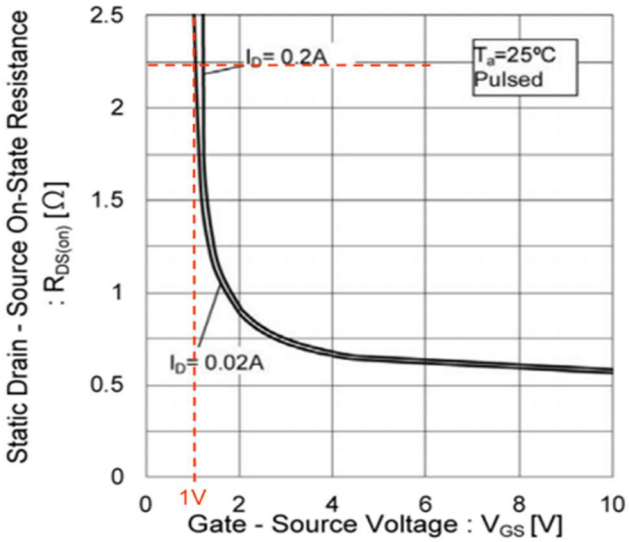

Figure 4.15 Static drain - source on-state resistance vs. gate source voltage from FET datasheet of RUC002N05.

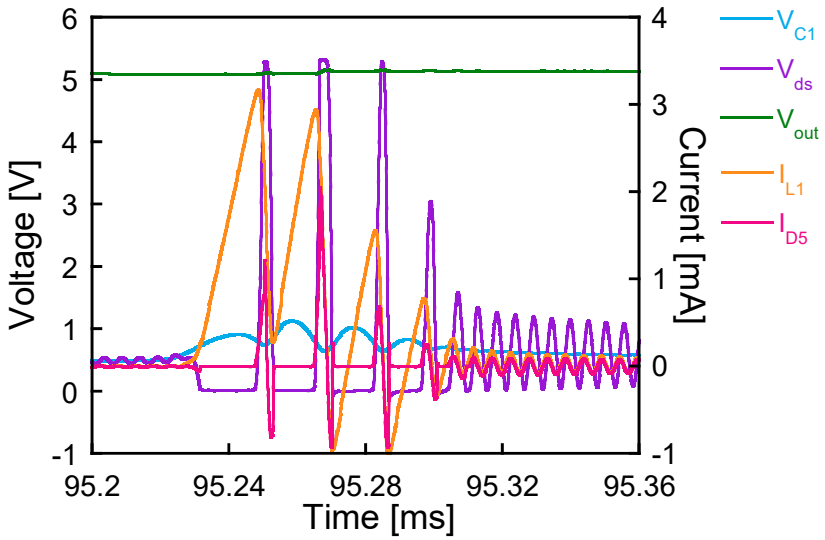

Figure 4.16 Simulated waveforms of the voltages and currents in the self-oscillating boost converter.

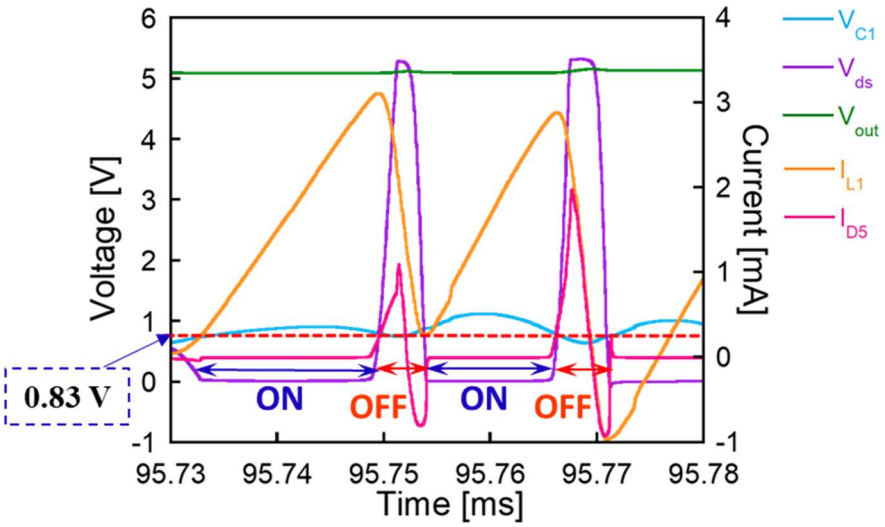

Figure 4.17 Enlarged view of simulated waveforms of the voltages and currents in the self-oscillating boost converter.

4.3.2 Circuit Parameters

Based on the aforementioned principle and simulation results, details regarding the parameters of the simulation circuit are listed in Table 4.2. The parameters summarized here are only used with the boost circuit discussed in Section 4.3.1 to obtain a stable 5 V voltage. If the output voltage value is changed, the corresponding parameters must be redesigned.

Table 4.2 Parameters of the circuit elements for the Wiegand pulse voltage with the self-oscillating boost converter.

Component	*Value*
Capacitance C1	20 nF
Inductance L1	4.5 mH
Capacitance C2	60 nF
Resistance R2	800 Ω
Diode	RBR3MM30A
MOSFET	RE1C002UN

V_{out} depends on the circuit parameters L_1 and C_1, as shown in Figure 4.18. V_{out} increases as C_1 decreases. The combination of L_1 = 4.5 mH and C_1 = 20 nF is optimum for producing a DC voltage of approximately 5.1 V, meeting the aim of this study to generate a DC voltage of 5 V, which can be used as a power source for several electronic modules. The dependency of the output voltage ripple on capacitor C_2 was also studied. As shown in Figure 4.19, V_{out} is not dependent on C_2, and it is stable with fewer ripples when C_2 > 60 nF.

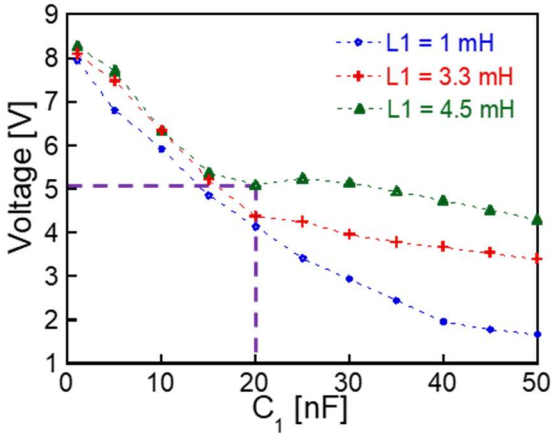

Figure 4.18 Dependence of the output voltage, V_{out}, on the parameters of L_1 and C_1.

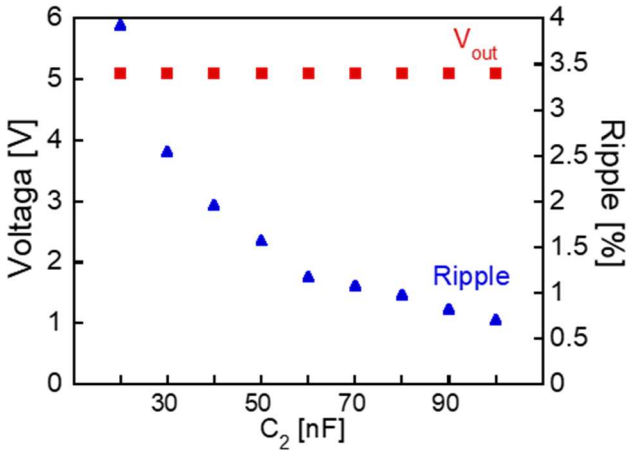

Figure 4.19 Output ripple voltage function of the output terminal C_2.

4.4 Verification of Self-Oscillating Boost Converter Circuit

4.4.1 Experimental Circuit

In this study, we used the electronic components in Table 4.2 to assemble the same experimental circuit as the simulation circuit. To reduce the loss caused by the parts in the circuit, small-signal corresponding components are used, such as FETs. All components are of the surface mount type and require the design of the printed circuit board to complete the experimental circuit. The experimental circuit is shown in Figure 4.20. The bridge rectifier of the diode is set on the leftmost side of the experimental circuit board, and the components of the boost circuit are set on the right: inductor, capacitor, FET, and diodes to prevent backflow. Compared to the wire connection of the electronic supplements, the assembly on the experimental board can minimize the direct wiring loss between the electronic components.

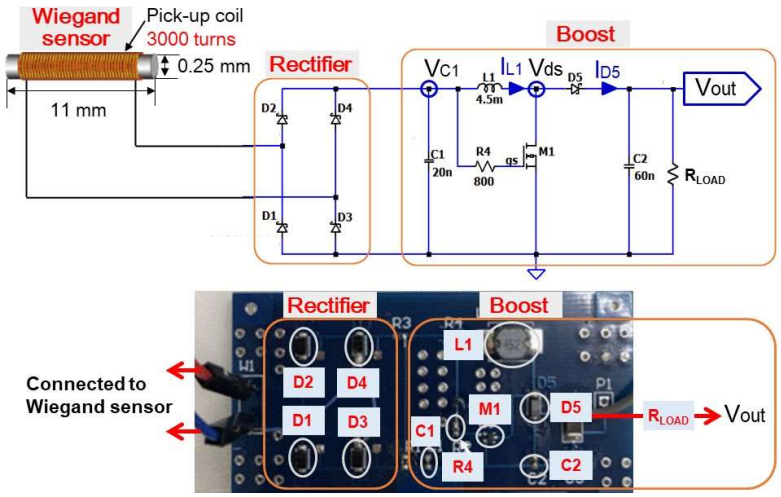

Figure 4.20 Experimental circuit for the Wiegand pulse voltage with self-oscillating boost converter.

4.4.2 Results of Output Voltage

When using a Wiegand sensor to provide energy without a power supply, the simplest traditional storage method is to use a capacitor. In this study, because the width of the Wiegand pulse voltage is short, the maximum energy cannot be absorbed within a short pulse voltage time; therefore, it is difficult to obtain the maximum output voltage. The input voltage with a peak value of 4.62 V can only be smoothed with a capacitor to obtain an output DC voltage of 2.77 V, which significantly reduces the power generation capacity of the Wiegand sensor harvester. In this chapter, we describe our design to obtain a stable output of 5 V using a self-oscillating boost converter without a power supply. First, LTspice® simulation was used to obtain a stable 5 V output voltage, and then the actual circuit verification was performed.

The self-oscillating boost converter presented in Section 4.2.2 was prototyped with the same components assumed in the LTspice® simulation and tested to experimentally assess its effectiveness as an energy harvester.

Figure 4.21 presents the experimental and simulated waveforms of the output and other voltages in the self-oscillating boost converter circuit shown in Figure 4.20 and Table 4.2. Because the applied field frequency was 1 kHz, the full-time scale of 0.5 ms in Figure 4.21 corresponds to one cycle of the generated Wiegand pulse. The observed oscillations of V_{ds}, V_{C1}, and V_{out} agree with those simulated.

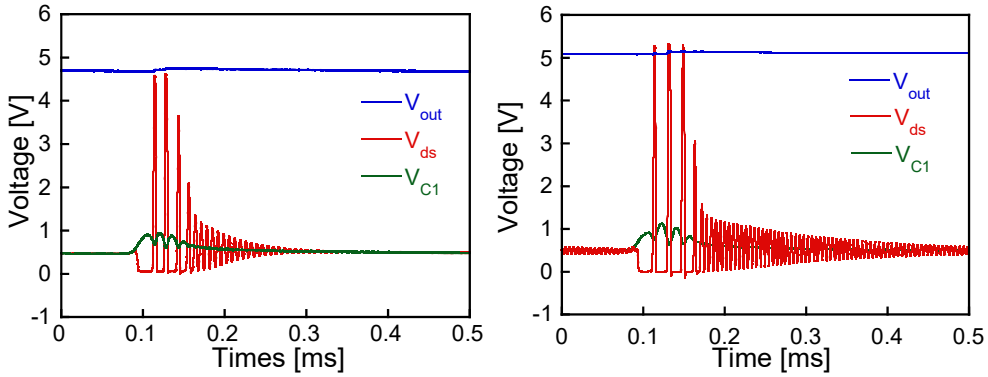

(a) Experimental waveforms (b) Simulated waveforms

Figure 4.21 Waveforms of V_{out}, V_{ds}, and V_{C1} in the self-oscillating boost converter.

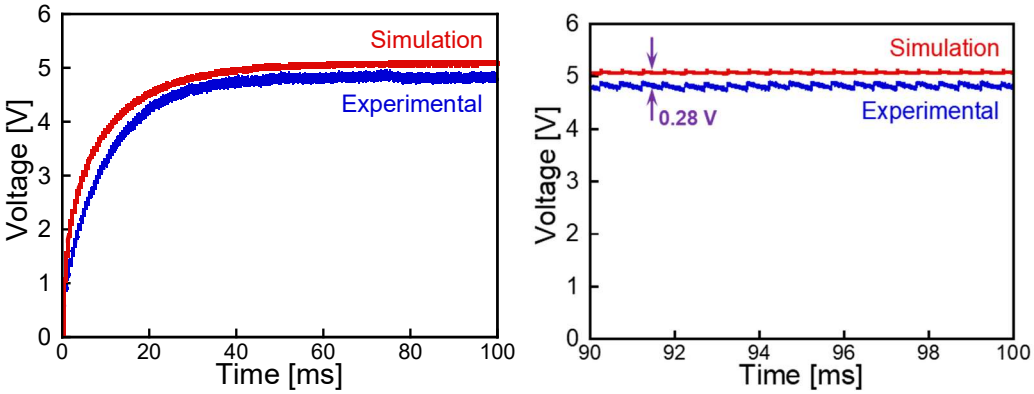

Figure 4.22 Simulated and experimental DC output voltage, V_{out}.

Figure 4.22 presents the time dependence of V_{out}. The simulated and observed saturated voltages are nearly equivalent. We discuss the experimental and simulated results of the circuit shown in Figure 4.20. The load resistance of R_3 = 5 MΩ was used, corresponding to a nearly "open circuit condition" for the output. In addition, owing to the loss of the actual circuit on the wiring board, the experimental output voltage was 0.28 V lower than that of the simulation result shown in Figure 4.22. The output voltages obtained by the experiment and simulation under the same parameters are similar, which prove the possibility of using the Wiegand sensor as a power source.

Figure 4.23 presents the electric power P_{out} utilized at R_{Load}. A maximum power of 63 μW was experimentally obtained at R_{Load} = 10 kΩ, which does not match the resistance of the pickup coil, such as 180 Ω of the Wiegand sensor. This mismatch is attributed to the elements and operation of the self-oscillating boost circuit. We have reported that the maximum power was obtained at a load resistance of 2 kΩ, which is higher than the DC coil resistance of the Wiegand sensor connected with the rectifying and smoothing circuits.

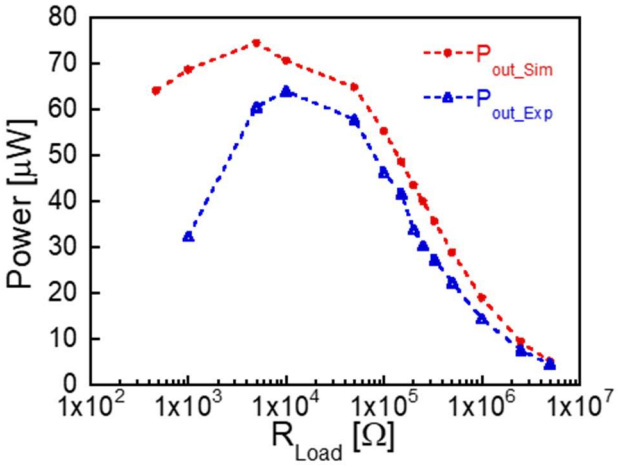

Figure 4.23 Dependence of the output power, P_{out}, on the load resistance, R_{Load}.

In this study, an externally applied alternating magnetic field was excited to generate a Wiegand pulse voltage. When the intensity of the magnetic field is constant, the frequency of the pulse voltage signal corresponds to the frequency of the alternating magnetic field, and the amplitude of the pulse voltage in each cycle is unchanged.[90, 91] When changing the frequency of the alternating magnetic field, which changes the frequency of the pulse signal, we need to determine the impact of the output voltage in the self-oscillating boost converter. In recent studies, Wiegand sensors have also been used at low frequencies. When the frequency of the external AC magnetic field excitation becomes low,[92-94] it is necessary to check the effect of the self-oscillating boost converter. Therefore, we will discuss the output voltage characteristics of 50–900 Hz .

Figure 4.24 presents the output voltage comparison when the external excitation frequency is 50–900 Hz. Here, as the frequency decreases, the output voltage level also decreases. When the frequency of the AC magnetic field is above 0.1 kHz, the ripple of the output voltage is very large, and the voltage is significantly low, which is difficult to use. When the frequency of the AC magnetic field is above 0.4 kHz, it can output a stable voltage higher than 3.3 V with a significantly small ripple. Generally, except for voltages below 3.3 V and special conditions, the ripple cannot exceed 10% of the output voltage. As shown in Figure 4.24, when the frequency of the AC magnetic field is above 0.3 kHz, the ripple rate does not exceed 10% of the output voltage, which can fully meet the design standards.

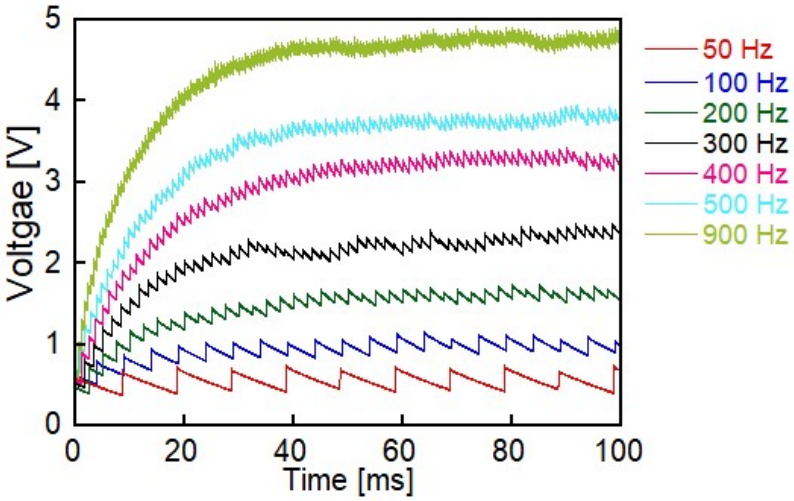

Figure 4.24 Dependences of the measured V_{out} on the frequency 50–900 Hz.

To understand the relationship between the frequency reduction and voltage, the relationship between the output voltage and ripple voltage from 50 Hz to 1 kHz is shown in Figure 4.25. As the frequency decreases, the output voltage also gradually decreases, and when the frequency changes, it is necessary to redesign the LC parameters to obtain a DC voltage of 5 V. This is sufficient to prove the versatility of the self-oscillating boost converter. We can design the required voltage value according to actual use and connect the control circuit to adjust the voltage. In this manner, we can obtain a stable DC output voltage through the designed circuit. Then, we discuss the maximum power that the circuit can provide under actual load conditions.

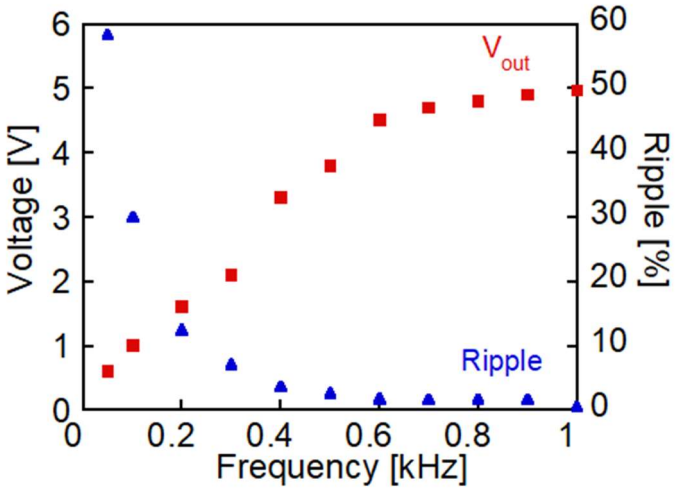

Figure 4.25 Dependence of the measured V_{out} on the frequency and its ripple rate.

In this study, an alternating magnetic field was externally applied to the Wiegand sensor as the excitation energy, generating the Wiegand pulse voltage. An attractive feature of the Wiegand sensor is that the generated pulse voltage is independent of the frequency of the applied alternating magnetic field. Figure 4.25 presents the measured V_{out} and its ripple rate function at an excitation frequency of 1 kHz and lower frequencies. V_{out} decreases with the frequency. However, a V_{out} of approximately 5 V and a low ripple rate are obtained in the frequency range down to 0.6 kHz. When the frequency is 0.4 kHz, the output voltage continues to reach 3.3 V with a ripple rate lower than 5%. This result indicates that the self-oscillating boost converter can be used for practical applications as a power source for electronic modules.

4.4.3 Results of Generated Power

The voltage with the load resistance is shown in Figure 4.26. When the load resistance is below 50 kΩ, the DC output cannot be obtained. On the other hand, the power generated by the Wiegand sensor is smaller than the power consumption of the load. All of the power is consumed by the load; therefore, the self-oscillating boost converter cannot work properly. Moreover, the electric power does not accumulate in the capacitor, and the load is not supplied with the necessary power. When the resistance value increases, the load current decreases, and the voltage obtained can be observed to be higher and more stable.

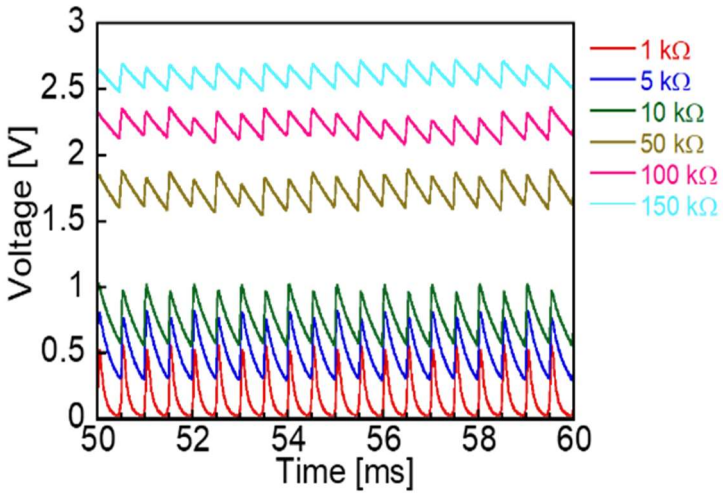

Figure 4.26 Output voltage with the load resistance.

Figure 4.27 presents the dependencies of I_{out} and V_{out} of the load resistance R_{Load} on R_{Load}. The simulation and actual experimental results are apparently identical. The maximum energy can be obtained as 4.63 μW, which verifies the practicality of the self-oscillating boost converter.

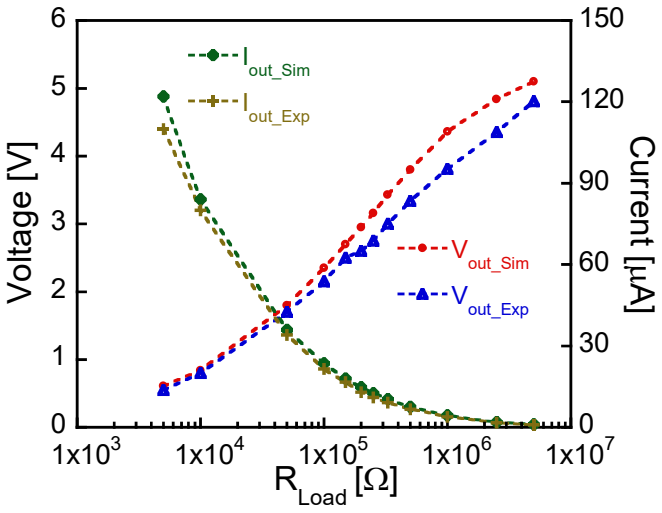

Figure 4.27 Dependences of the simulated and measured V_{out} and I_{out} on the load resistance, R_{Load}.

4.4.4 Application for Self-powered Modules

In the case of load resistance, the change in the power obtained by the different frequencies is also considered. In the previous section, we verified that a smooth DC voltage can be obtained at 100 Hz without changing the parameters of the self-oscillating boost circuit. This demonstrates that the self-exciting boost circuit is also suitable for low-frequency applications.

Figure 4.28 summarizes the relationship between V_{out} and I_{out} obtained using the Wiegand sensor with a self-oscillating boost converter. It presents the voltage and current range functions of the load resistance used for practical applications as power sources. A stable output of 5 V is maintained for currents up to 1 μA. This voltage/current range is used in low-energy IoT devices,[95, 96] such as significantly low-power microcontrollers and radio frequency circuits for a power supply. Practical design ideas are obtained in this study. With the upgrade of electronic products, the application of this μW energy will become increasingly extensive. Furthermore, it is compatible with the existing energy harvesting IC, such as the power-storing buck DC–DC converter used for photovoltaic and vibration power generation elements.[97, 98] Typically, a DC–DC converter is used in combination with storage batteries to ensure a high efficiency and a maximum current supply of 1 mA.[99, 100] Therefore, the circuit system with the Wiegand sensor developed in this study can be used with a storage battery. It allows a higher capability of current consumption and can be used as a power supply for IoT devices.

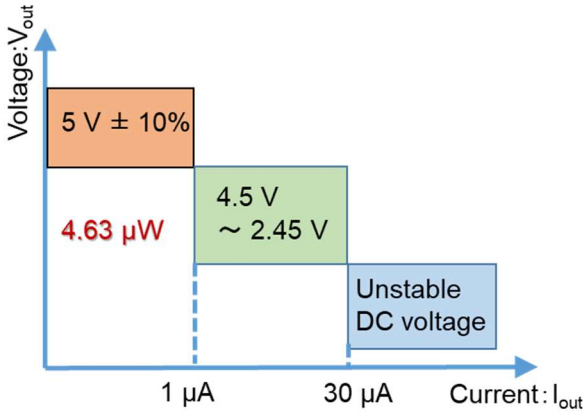

Figure 4.28 Mapping of V_{out} - I_{out} for practical applications of the Wiegand sensor with a self-oscillating boost converter.

4.5 Summary

In this chapter, we discussed that the simplest smoothing capacitor can obtain a stable voltage of 2.77 V following a full-wave bridge rectifier. However, the general IoT application voltage is 3.3 V or 5 V; therefore a DC voltage of 2.77 V cannot be used for IoT devices. Here, we used a self-oscillating boost converter circuit to effectively solve the boost problem. We proved the versatility of the boost circuit despite the Wiegand pulse voltage frequency being different. When changing the frequency, it is necessary to adjust the LC parameters appropriately to boost the voltage. If the IoT sensor is determined, the boost circuit can be used to provide the voltage. Therefore, we discussed the case in which the boost circuit can provide energy, which is acceptable for IoT applications that consume less than 4.63 μW. Finally, we compared the power-storing buck DC–DC converter and proposed a solution to increase the consumption current, which is to use the storage battery to store the energy obtained by the self-oscillating boost converter.

Chapter 5: Conclusion

With the development of the IoT society, the number of IoT devices is growing at a fast pace. These devices require a significant number of batteries that costly and time-consuming maintenance. Therefore, autonomous power generation facilities with battery-less and maintenance-free equipment are needed to meet the ever-increasing demand for IoT devices. And with the development of miniaturization and energy-saving, low-power power supplies can gradually meet several applications of IoT devices. This research proposes a new method of electricity generation using a Wiegand sensor as an energy harvesting element. So we used the electromagnetic induction method of the Wiegand sensor, which induces the frequency-independent pulse voltage, to develop battery-less power generation modules.

In this study, an alternating magnetic field of 3.2 kA/m at 1 kHz was applied to the Wiegand sensor, and alternating positive and negative pulse voltages (V_{open}) were induced to the pickup coil. Due to the internal resistance and inductance of the Wiegand wire and the pickup coil, V_{open} is inaccurate when used in the power supply voltage. Here, we propose a concept of obtaining the inherent pulse voltage from Wiegand sensor as the power source, and verified its effectiveness in circuit simulation. Using MATLAB®/Simulink® simulation, we determined the circuit parameters of the internal resistance and inductance of the pickup coil, and used the time correlation (waveform) of the pulse voltage as the inherent pulse voltage (V_{in}). As an example of circuit simulation, the circuit response through a full-wave bridge rectifier circuit connected to a Wiegand sensor was calculated. The calculated output voltage is consistent with the experimental measurement value, and proves the effectiveness of using the inherent pulse voltage and the internal resistance and inductance of the Wiegand sensor.

Then inherent pulse voltage (V_{in}) from the Wiegand sensor needs to be converted to a DC power voltage for IoT devices. In DC conversion experiments, the maximum DC voltage of 2.77 V can be obtained from the Wiegand sensor through full-wave bridge rectifier and smoothing of capacitors. In order to be more widely used in the power of IoT device, it is necessary to convert the Wiegand pulse voltage into a 5 V DC voltage which can be applied to a variety of electronic modules. In the absence of an external power supply, we use a self-oscillating boost converter circuit to obtain a DC voltage of 5 V. Moreover, the experimental results are consistent with the simulation on the voltage/current and ripple characteristics, which are sufficient to verify the design accuracy of the 5 V self-oscillating boost converter circuit.

Under actual application conditions, the Wiegand pulse voltage frequency is different, so we also proved that this boost circuit is also effective when changing the frequency. And we have determined that the boost circuit can provide energy for IoT devices that consume less than 4.63 μW. Finally, a solution applied to power consumption that higher than 4.63 μW is proposed, that is, increase the energy obtained by combining the storage battery.

The related method of Wiegand sensor utilization as a power source and the connection circuit for obtaining energy here are expected to be used in the application of IoT devices. This research provides a significant development for Wiegand sensors used as power sources for battery-less devices and modules.

Acknowledgement

First of all, I would like to express my deepest gratitude to Professor Yasushi Takemura for his continuous encouragement and guidance. I am also grateful to the members of the Wiegand Sensor & Circuit team for their practical advices in this study.

Finally, I want to express my greatest gratitude to my family for their support.

References

1. S. Balakrishna, M. Thirumaran, V. K. Solanki, “A framework for IoT sensor data acquisition and analysis”, *EAI Endorsed Transactions on Internet of Things*, Vol. 4, pp. 1-13, 2018.

2. D. Singh, G. Tripathi, A. J. Jara, “A survey of Internet-of-Things: Future vision, architecture, challenges and services”, *IEEE World Forum on Internet of Things*, pp. 287-292, 2014.

3. R.J.M. Vullers, R. V. Schaijk, H. J. Visser, J. Penders, C. V. Hoof, “Energy harvesting for autonomous wireless sensor networks”, *IEEE Sol. Sta. Cir. Mag*., Vol. 2, pp. 29-38, 2010.

4. S. C. Lai, K. Yao, C. Y. Tan, “A Battery-less sensor concept outputting perceivable signal demonstrated with an accelerometer”, *IEEE Sensors Journal*, Vol. 16, No. 22, pp. 7841-7842, 2016.

5. T. S. Muratkar, A. Bhurane, A. Kothari, “Battery-less Internet of Things -A Survey”, *Computer Networks*, Vol. 180, pp. 1-20, 2020.

6. T. Armstong, “Green Buildings Get a Boost: Wireless sensor nodes as a key application for energy harvesting”, Analog Devices, Available online: https://www.analog.com/media/en/technical-documentation/tech-articles/green-buildings-get-a-boost.pdf, accessed Mar. 6, 2021.

7. H. Jayakumar, A. Raha, Y. Kim, S. Sutar, W. S. Lee, V. Raghunathan, “Energy-efficient system design for IoT devices”, *Asia & South Pacific Design Automation Conference*, pp. 298-301, 2016.

8. R.J.M. Vullers, R. V. Schaijk, I. Doms, C. V. Hoof, R. Mertens, “Micropower energy harvesting”, *Solid-State Electronics*, Vol. 53, pp. 684-693, 2009.

9. J. A. Paradiso, T. Starner, “Energy scavenging for mobile and wireless electronics”, *IEEE Pervasive Computing*, Vol. 4, No. 1, pp. 18-27, 2005.

10. N. Sharpes, D. Vuckovic, S. Priya, “Floor Tile Energy Harvester for Self-Powered Wireless Occupancy Sensing”, *Energy Harvesting and Systems*, Vol. 3, pp. 43-60, 2015.

11. A.A.A. Rahman, N. A. Rashid, A.S.A. Aziz, G. Witjaksono, “Design of autonomous micro-solar powered energy harvesting system for self-powered batteries-less wireless sensor mote”, *Electronics Goes Green 2012+ (EGG)*, pp. 1-4, 2012.

12. G. Kuers, H. -J. Gevatter, “Wiegand-Sensoren für Weg- und Geschwindigkeitsmessungen/ Wiegand effect position and speed sensors”, *Technisches Messen 51*, Vol. 4, pp. 123-129, 1984.

13. K. Takahashi, A. Takebuchi, T. Yamada, Y. Takemura, “Power supply for medical implants by Wiegand pulse generated from a magnetic wire”, *J. Mag. Soc. Jpn.*, Vol. 42, pp. 49-54, 2018.

14. R. Zentgraf, D. Hennig, “Evaluation of self-sufficient zero speed sensors based on Large Barkhausen jumps”, *20th International Student Conference on Electrical Engineering*, Prague, 2016.

15. H. Guenther, J. Holger, “Movement sensor esp. for bicycle tachometer - uses magnets on spokes generating alternating magnetic field w.r.t. fixed Wiegand element”, German Patent # DE4007653, 1991.

16. D. J. Dlugos, D. Small, D. A. Siefer, “Wiegand effect energy generator”, U.S. Patent #6,191,687,B1, 2001.

17. T. Best, “Wiegand Wire: Energy Harvesting and More”, Techbriefs, Available online: https://www.techbriefs.com/component/content/article/tb/supplements/md/features/articles/37387, accessed Jun. 25, 2021.

18. J. Taneja, J. Jeong, D. Culler, “Design, Modeling, and Capacity Planning for Micro-solar Power Sensor Networks”, *2008 International Conference on Information Processing in Sensor Networks*, pp. 407-418, 2008.

19. Y. Li, L. Wu, C. Zhang, Z. Wang, “Power recovery circuit for Battery-less TPMS”, *2007 7th International Conference on ASIC*, pp. 454-457, 2007.

20. J. E. Opie, J. W. Bossoli, “A new era of application for the Wiegand effect”, *SAE Transactions*, Vol. 97, pp. 426-431, 1988.

21. C. Luo, H. F. Hofmann, “Wideband energy harvesting for piezoelectric devices with linear resonant behavior”, *IEEE Transactions on Ultrasonics*, *Ferroelectrics & Frequency Control*, Vol. 58, No. 7, pp. 1294-1301, 2011.

22. POSITAL-FRABA. “Wiegand technology”, Available online: https://www.posital.com/en/products/wiegand-sensors/wiegand-techology.php, acessed Mar. 6, 2021.

23. C. Knight, J. Davidson, S. Behrens, “Energy Options for Wireless Sensor Nodes”, *Sensors*, Vol. 8, pp. 8037-8066, 2008.

24. H. Morimura, S. Oshima, K. Matsunaga, T. Shimamura, M. Harada, “Ultra-low-power circuit techniques for mm-size wireless sensor nodes with energy harvesting”, *IEICE Electronics Express*, Vol. 11, No. 20, pp. 1-12, 2014.

25. Y. Chen, Z. Jiao, W. Guan, Q. Sun, X. Wang, R. Zhang, H. Zhang, “A +0.66/−0.73 ℃ inaccuracy, 1.99-μw time-domain CMOS temperature sensor with second-order ΔΣ modulator and on-chip reference clock”, *IEEE Transactions on Circuits and Systems I: Regular Papers*, Vol. 67, No, 11, pp. 3815-3827, 2020.

26. J.M.D. Coey, “Magnetism and Magnetic Materials”, Cambridge University Press, 2010.

27. N. A. Spaldin, “Magnetic Materials: Fundamentals and Applications (2nd Edition)”, Cambridge University Press, 2010.

28. E. M. Purcell, “Electricity and Magnetism (Berkeley Physics Course)”, McGraw-Hill Science Engineering, 1984.

29. J. R. Wiegand, M. Velinsky, “Bistable magnetic device”, U.S. Patent #3,820,090, 1974.

30. J. R. Wiegand, “Switchable magnetic device”, U.S. Patent # 4,247,601, 1981.

31. N. Normann, “Magnetic field sensor comprising Wiegand wires or similar bistable magnetic elements”, U.S. Patent # 4,639,670, 1987.

32. K. Thapa, “Making switches smarter with true micropower Hall effect sensors”, *Electronic Product Design*, Vol. 12, pp. 14-15, 2016.

33. C. T. Horng, R. Xiao, R. Y. Tong, J. W. Chang, K. Ju, S. H. Liao, “Anisotropic magnetoresistive (MR) sensor element with enhanced magnetoresistive (MR) coefficient”, U.S. Patent # 6,590,751, 2003.

34. S. Abe, A. Matsushita, “Induced pulse voltage in twisted Vicalloy wire with compound magnetic effect”, *IEEE Transactions on Magnetics*, Vol. 31, No. 6, pp. 3152-3154, 1995.

35. POSITAL-FRABA, “Innovative encoders for demanding applications”, Available online: https://pr-toolbox.com/pdf/FRABA_AbsoluteEncoders.pdf, accessed Mar. 6, 2021.

36. S. Abe, A. Matsushita, “Construction of electromagnetic rotation sensor using compound magnetic wire and measurement at extremely low frequency rotations”, *IEEE Transactions on Magnetics*, Vol. 30, No. 6, pp. 4635-4637, 1994.

37. A. Takebuchi, T. Yamada, Y. Takemura, “Reduction of vibration amplitude in vibration-type electricity generator using magnetic wire”, *Journal of the magnetics Society of Japan*, Vol. 41, pp. 34-40, 2017.

38. K. J. Sixtus, L. Tonks, “Propagation of large Barkhausen discontinuities”, *Phys. Rev*, Vol. 37, pp. 930-959, 1931.

39. K. J. Sixtus, L. Tonks, “Propagation of large Barkhausen discontinuities II”, *Phys. Rev*, Vol. 42, pp. 419-435, 1932.

40. J. Chotai, M. Thakker, Y. Takemura, “Single-bit, Self-powered digital counter using a Wiegand sensor for rotary applications”, *Sensors*. Vol. 20, 3840, pp. 1-10, 2020.

41. M. Vazquez, C. Gomez-Polo, D. -X. Chen, A. Hernando, “Magnetic bistability of amorphous wires and sensor applications”, *IEEE Transactions on Magnetics*, Vol. 30, No. 2, pp. 907-912, 1994.

42. Y. Takemura, T. Aoki, H. Tanaka, T. Yamada, S. Abe, S. Kohno, H. Nakamura, “Control of demagnetizing field and magnetostatic coupling in FeCoV wires for zero-speed sensor”, *IEEE Transactions on Magnetics*, Vol. 42, No. 10, pp. 3300-3302, 2006.

43. H. Tanaka, T. Yamada, Y. Takemura, S. Abe, S. Kohno, H. Nakamura, “Constant velocity of domain wall propagation independent of applied field strength in vicalloy wire”, *IEEE Transactions of Magnetics*, Vol. 43, No. 6, pp. 2397-2399, 2007.

44. A. Matsushita, Y. Takemura, “Power generating device using compound magnetic wire”, *Journal of Applied Physics*, Vol. 87, pp. 6307-6309. 2000.

45. A. Matsushita, S. Abe, S. Ishida, C. F. Jie, “Magnetization reversal and domain wall propagation characteristics of compound magnetic wire”, *IEEE Translation Journal on Magnetics in Japan*, Vol. 6, No. 5, pp. 415-421, 1991.

46. T. Kohara, T. Yamada, S. Abe, S. Kohno, F. Kaneko, Y. Takemura, “Effective excitation by single magnet in rotation sensor and domain wall displacement of FeCoV wire”, *Journal of Applied Physics*, Vol. 109, 07E531, 2011.

47. R. Gherca, R. Olaru, “Harvesting vibration energy by electromagnetic induction”, *Annals of the University of Craiova*, *Electrical Engineering series*, No. 35, pp. 1842-4805, 2011.

48. K. Makihara, J. Onoda, T. Miyakawa, “Low energy dissipation electric circuit for energy harvesting”, *Smart Mater. Struct.*, Vol. 15, No. 5, pp. 1493-1498, 2006.

49. N. Kularatna, K. Subasinghage, K. Gunawardane, D. Jayananda, T. Ariyarathna, “Supercapacitor assisted techniques and supercapacitor assisted loss management concept: new design approaches to change the roadmap of power conversion systems”, *Electronics 2021*, Vol. 10, pp. 1-19, 2021.

50. K. Kankanmage, N. Kulatana, “Supercapacitor assisted LDO (SCALDO) technique an extra low frequency design approach to high efficiency DC-DC converters and how it compares with the classical switched capacitor converters”, *2013 Twenty-Eighth Annual IEEE Applied Power Electronics Conference and Exposition (APEC) IEEE*, pp. 1979-1984, 2013.

51. C. Renner, S. Unterschütz, V. Turau, K. Römer, “Perpetual data collection with energy-harvesting sensor networks”, *ACM Trans. Sensor Netw.*, Vol. 11, No. 1, Article 12, pp.1-12, 2014.

52. T. F. Valone, G. A. Robertson, “Permanent Magnet Spiral Motor for Magnetic Gradient Energy Utilization: Axial Magnetic Field”, *American Institute of Physics*, pp.1-12, 2010.

53. N. Khosropour, F. Krummenacher, M. Kayal, “Fully integrated ultra-low power management system for micro-power solar energy harvesting applications”, *Electronics Letters*, Vol. 48, pp. 338-339, 2012.

54. F. Ongaro, S. Saggini, P. Mattavelli, “Li-ion battery-supercapacitor hybrid storage system for a long lifetime, photovoltaic-based wireless sensor network”, *IEEE Trans. Power Electron.*, Vol. 27, No. 9, pp. 3944-3952, 2012.

55. A. Khaligh, P. Zeng, C. Zheng, “Kinetic energy harvesting using piezoelectric and electromagnetic technologies-State of the art”, *IEEE Trans. Ind. Electron.*, Vol. 57, No. 3, pp. 850-860, 2010.

56. A. Shareef, W. L. Goh, S. Narasimalu, Y. Gao, “A rectifier-less AC-DC interface circuit for ambient energy harvesting from low-voltage piezoelectric transducer array”, *IEEE Transactions on Power Electronics*, Vol. 34, No. 2, pp. 1446-1457, 2019.

57. M. Ericka, D. Vasic, F. Costa, G. Poulin, S. Tliba, “Energy harvesting from vibration using a piezoelectric membrane”, *Journal De Physique IV*, Vol. 128, pp. 187-193, 2005.

58. Y. Takemura, N. Fujinaga, A. Takebuchi, T. Yamada, “Battery-less hall sensor operated by energy harvesting from a single Wiegand pulse”, *IEEE Transactions on Magnetics*, Vol. 53, No. 11, 4002706, 2017.

59. T. Kohara, T. Kusunoki, T. Yamada, T. Suzuki, H. Fujimoto, Y. Takemura, S. Abe, S. Kohno, H. Itoi, F. Kaneko, “Fabrication and implementation of a rotation sensor using a separated structure consisting of magnetic wire and a pick-up coil”, *Journal of the Magnetics Society of Japan*, Vol. 34, pp. 347-351, 2010.

60. R. Malmhall, K. Mohri, F. B. Humphrey, T. Manabe, H. Kawamura, J. Yamasaki, I. Ogasawara, “Bistable magnetization reversal in 50 μm diameter annealed cold drawn amorphous wires”, *IEEE Transactions on Magnetics*, Vol. 23, No. 5, pp. 3242-3244, 1987.

61. S. Abe, A. Matsushita, M. Naoe, “Annealing and torsion stress effect on magnetic anisotropy and magnetostriction of Vicalloy fine wire”, *IEEE Transactions on Magnetics*, Vol. 33, pp. 3916-3918, 1997.

62. C. Yang, T. Sakai, T. Yamada, Z. Song, Y. Takemura, “Improvement of pulse voltage generated by wiegand sensor through magnetic-flux guidance”, *Sensors*, Vol. 20, 1408, pp. 1-10, 2020.

63. A. A. Trofimov, N. S. Trifomova, S. A. Zdobnov, D. V. Popchenkov, K. I. Bastrygin, A. K. Alimuradov, “Construction of rotational speed sensors based on the Wiegand module”, *2020 Moscow Workshop on Electronic and Networking Technologies (MWENT)*, pp. 1-4, 2020.

64. S. Saggini, F. Ongaro, L. Corradini, A. Affanni, “Low-power energy harvesting solutions for wiegand transducers”, *IEEE J. Eme. Sel. Top. Pow. Ele.*, Vol. 3, pp. 766-779, 2015.

65. K. Takahashi, T. Yamada, Y. Takemura, “Circuit parameters of a receiver coil using a Wiegand sensor for wireless power transmission”, *Sensors*, Vol. 19, 2710, pp.1-9, 2019.

66. E. Lefeuvre, D. Audigier, C. Richard, D. Guyomar, “Buck-boost converter for sensorless power optimization of piezoelectric energy harvester”, *IEEE Trans. Power Electron.*, Vol. 22, No. 5, pp. 2018-2025, 2007.

67. J. Liang, W. H. Liao, “Improved design and analysis of self-powered synchronized switch interface circuit for piezoelectric energy harvesting systems”, *IEEE Trans. Ind. Electron.*, Vol. 59, No. 4, pp. 1950-1960, 2012.

68. E. Arroyo, A. Badel, F. Formosa, “Energy harvesting from ambient vibrations: Electromagnetic device and synchronous extraction circuit”, *Journal of Intelligent Material Systems and Structures*, Vol. 24, pp. 2023-2035, 2013.

69. V. Ostasevicius, V. Markevicius, V. Jurenas, M. Zilys, M. Cepenas, L. Kizauskiene, V. Gyliene, “Cutting tool vibration energy harvesting for wireless sensors applications”, *Sensors and Actuators A: Physical*, Vol. 233, pp. 310-318, 2015.

70. ROHM, “RBR3MM30x datasheet”, Available online: https://d1d2qsbl8m0m72.cloudfront.net/en/products/databook/datasheet/discrete/diode/schottky_barrier/rbr3mm30atr-e.pdf, accessed Mar. 18, 2021.

71. P. E. Wigen, “Wiegand wire: New material for magnetic-based devices”, *Electronics*, Vol. 30, pp. 350-352, 1975.

72. A. D. Nath, K. Radhakrishnan, K. A. Eldhose, “Low-Voltage direct AC-DC boost converter for micro-generator based energy harvesting”, *International Journal of Advanced Research in Electrical Electronics & Instrumentation Engineering* , Vol. 2, pp. 2320-3765, 2013.

73. A.H.A. Dawam, M. Muhamad, “AC to DC bridgeless boost converter for ultra-low input energy harvesting”, *IOP Conference Series: Materials Science and Engineering*, Vol. 341, 012001, pp. 1-7, 2018.

74. S. Dwari, L. Parsa, “Efficient low voltage direct AC/DC converters for self-powered wireless sensor nodes and mobile electronics”, *INTELEC 2008 - 2008 IEEE 30th International Telecommunications Energy Conference*, pp. 1-7, 2008.

75. D. Guyomar, A. Badel, E. Lefeuvre, C. Richard, “Toward energy harvesting using active materials and conversion improvement by nonlinear processing”, *IEEE Trans. Ultrason.*, *Ferroelect.*, Vol. 52, No. 4, pp. 584-595, 2005.

76. J. Liang, W. Liao, “An improved self-powered switching interface for piezoelectric energy harvesting”, *2009 International Conference on Information and Automation*, pp. 945-950, 2009.

77. G. K. Ottman, H. F. Hofmann, G. A. Lesieutre, “Optimized piezoelectric energy harvesting circuit using step-down converter in discontinuous conduction mode”, *IEEE Trans. Power Electron.*, Vol. 18, No. 2, pp. 696-703, 2003.

78. Texas Instruments, “Practical feedback loop analysis for voltage-mode boost converter”, Available online: https://www.ti.com/lit/an/slva633/slva633.pdf, accessed Mar. 12, 2021.

79. Linear Technology, “LTC3588-1 datasheet”, Available online: https://www.analog.com/media/en/technical-documentation/data-sheets/35881fc.pdf, accessed Mar. 18, 2021.

80. Linear Technology, “LTC3400 datasheet”, Available online: https://www.analog.com/media/en/technical-documentation/data-sheets/3400fa.pdf, accessed Jun. 25, 2021.

81. E. Rogers, “Control loop modeling of switching power supplies”, Available online: https://www.ti.com/sc/docs/msp/papers/1998/rogers.pdf, accessed Mar. 23, 2021.

82. L. Shtargot, “Micropower SOT-23 boost with integrated schottky diode provides output disconnect and short circuit protection”, Available online: https://www.analog.com/en/technical-articles/micropower-sot23-boost-integrated-schottky-diode.html, accessed Mar. 23, 2021.

83. A. I. Pressman, K. Billings, T. Morey, “Switching Power Supply Design, 3rd Ed”, McGraw-Hill Education, pp. 31-42, 2009.

84. C. Nelson, J. Williams, “LT1070 design manual”, Available online: https://www.analog.com/media/en/technical-documentation/application-notes/an19fc.pdf, accessed Mar. 6, 2021.

85. S. Subi, “ZCS-PWM converter for reducing switching losses”, *IOSR Journal of Electrical and Electronics Engineering*, Vol. 9, pp. 29-35, 2014.

86. E. Van Dijk, H.J.N. Spruijt, D. M. O’Sullivan, J. B. Klaassens, “PWM-switch modeling of DC–DC converters”, *IEEE Transactions on Power Electronics*, Vol. 10, No. 6, pp. 659-665, 1995.

87. S. Nakagawa, “A voltage step down type dc-dc converter having a coupled inductore”, European Patent Application #EP1126585A2, 2001.

88. R. W. Erickson, “DC–DC power converters”, *Wiley Encyclopedia of Electrical and Electronics Engineering*, pp. 1-18, 2007.

89. ROHM, “RE1C002UN datasheet”, Available online: https://www.alldatasheet.com/datasheet-pdf/pdf/1070449/ROHM/RE1C002UN.html, accessed Mar. 18, 2021.

90. C -C. Chang, J -Y. Chang, “Novel Wiegand effect based energy harvesting device for linear positioning measurement system”, *Microsystem Technologies*, Vol. 26, pp. 3421-3426, 2020.

91. POSITAL-FRABA, “Wiegand energy harvesting”, Available online: https://www.posital.com/en/products/wiegand-sensors/wiegand-energy-harvesting.php, accessed Mar. 6, 2021.

92. Y. Takemura, A. Matsushita, “Frequency dependence of output voltage generated from bundled compound magnetic wires”, *IEEE Transactions on Magnetics*, Vol. 37, No. 4, pp. 2862-2864, 2001.

93. K. Mohri, S. Takeuchi, T. Fujimoto, “Sensitive magnetic sensors using amorphous Wiegand-type ribbons”, *IEEE Transactions on Magnetics*, Vol. 17, No. 6, pp. 3370-3372, 1981.

94. ICNIRP: “Guidelines for limiting exposure to time varying electric and magnetic fields (1 Hz-100 kHz)”, *Health Phys.*, Vol. 99, No. 6, pp. 818-836, 2010.

95. Texas Instruments, “Energy harvesting for wireless switch power reference design”, Available online: https://www.ti.com/lit/ug/tiduc93/tiduc93.pdf, accessed Mar. 21, 2021.

96. D. Newell, M. Duffy, “Review of power conversion and energy management for Low-Power, Low-Voltage energy harvesting powered wireless sensors”, *IEEE Trans. Power Electron.*, Vol. 34, No. 10, pp. 9794-9805, 2019.

97. Texas Instruments, “TPS6273x datasheet”, Available online: http://www.ti.com/lit/ds/symlink/tps62730.pdf, accessed Mar. 12, 2021.

98. R1801K, Available online: https://www.mouser.co.uk/datasheet/2/792/r1801k001a_eev-1917814.pdf, accessed Mar. 26, 2021.

99. J. Drew, “Powering a Dust Mote from a Piezoelectric Transducer”, Available online: https://www.analog.com/jp/technical-articles/powering-a-dust-mote-from-a-piezoelectric-transducer.html, accessed Mar. 26, 2021.

100. Texas Instruments, “Energy Harvesting ULP meets energy harvesting: A game-changing combination for design engineers”, Available online: https://www.mouser.com/pdfDocs/TI-ULP-meets-energy-harvesting-A-game-changing-combination-for-design-engineers.pdf, accessed Jun. 25, 2021.

Publications

[Papers]

[1] Xiaoya Sun, Tsutomu Yamada, Yasushi Takemura
"Output characteristics and circuit modeling of Wiegand sensor"
Sensors (Q1, IF=3.275), Vol. 19, Iss. 13, 2991, pp. 1-9, 2019.
DOl: 10.3390/S19132991

[2] Xiaoya Sun, Haruchika Iijima, Stefano Saggini, Yasushi Takemura
"Self-oscillating boost convert of Wiegand pulse voltage for self-powered modules"
Energies (Q1, IF=3.004), Vol. 14, Iss. 17, 5373, pp. 1-11, 2021.
DOl: 10.3390/en14175373

[International Conferences]

[1] Takafumi Sakai, Xiaoya Sun, Yasushi Takemura
"Power generation for battery-less sensor operation and wireless power transfer using Wiegand sensor"
Magnetic Frontiers 2019: Magnetic Sensors, Lisbon, Portugal, June 24-27, 2019.

[国内学会]

[1] 飯島榛史、孫小雅、原和江、酒井貴史、山田努、竹村泰司
"磁性ワイヤ・コイル分離型 Wiegand センサを用いた振動発電と等価回路解析"
第 43 回日本磁気学会学術講演会、25pD-3、京都、2019 年 9 月 25-27 日.